

Advection–diffusion-limited dissolution

Chris H. Rycroft^{a,b}, Martin Z. Bazant^{c,d}

^a*School of Engineering and Applied Sciences, Harvard University, Cambridge, MA 02138*

^b*Department of Mathematics, Lawrence Berkeley Laboratory, Berkeley, CA 94720*

^c*Department of Chemical Engineering, Massachusetts Institute of Technology, MA 02139*

^d*Department of Mathematics, Massachusetts Institute of Technology, MA 02139*

Abstract

An advection–diffusion-limited dissolution model of an object being eroded by a two-dimensional potential flow is presented. By taking advantage of conformal invariance of the model, a numerical method is introduced that tracks the evolution of the object boundary in terms of a time-dependent Laurent series. Simulations of several dissolving objects are shown, which shrink and then collapse to a single point in finite time. The simulations reveal a surprising exact relationship whereby the collapse point is the root of a non-analytic function given in terms of the flow velocity and the Laurent series coefficients describing the initial shape. This result is subsequently derived using residue calculus. The structure of the non-analytic function is examined for three different test cases, and a practical approach to determine the collapse point using a modified Newton–Raphson root-finding algorithm is outlined.

Keywords: conformal mapping, interfaces

1. Introduction

Interfacial growth processes, such as alloy solidification [1, 2, 3, 4], electrodeposition [5, 6], and crystal formation [7, 8], are responsible for a wide variety of complex natural patterns [9, 10] that emerge due to instabilities in the underlying equations for interface motion [11, 12]. A particularly well-studied model of interfacial growth is diffusion-limited aggregation (DLA) [13], where a solid cluster is grown starting from a single static particle. Additional particles are introduced far away from the cluster, carry out random walks, and adhere to the cluster upon contact, causing it to grow. Since a random walker is more likely to first meet an extremity of the cluster than an interior region, the extremities grow preferentially, leading to complex fractal clusters in discrete computer simulations of the model [13, 14, 15, 16].

Diffusion-limited aggregation has also been studied in the continuum limit, whereby the steady-state walker concentration satisfies Laplace’s equation outside the cluster, is zero on the cluster boundary, and tends to a steady concentration far away from the cluster. The growth rate of the cluster boundary is proportional to the normal gradient of the walker concentration. This problem is conformally invariant, which simplifies the analysis and allows it to be studied in detail in two

Email addresses: chr@seas.harvard.edu (Chris H. Rycroft), bazant@mit.edu (Martin Z. Bazant)

dimensions using conformal mapping. Continuum DLA is also unstable, and perturbations in an object's boundary sharpen over time and eventually lead to cusps [17]. There is a close parallel between continuum DLA and viscous fingering [18], which can be modeled in terms of a conformally invariant equations for the fluid pressure [19, 20, 21], resulting fractal shapes with a very similar morphology to DLA [22].

While discrete DLA can be simulated on lattices, an alternative numerical approach is to exploit the conformal invariance of the problem, and define the growing cluster using a chain of conformal maps that each add a small bump to the shape, corresponding to a single particle aggregating [23]. The use of conformal maps opens up other possibilities, such as growing non-random clusters [24]. A further extension is to the case where the diffusing particles are transported by a fluid potential flow around the growing cluster, which is made possible because the advection–diffusion equation for the walker concentration is also conformally invariant [25, 26]. For this model, an asymptotic analysis of the walker concentration has been studied [27], the discrete and continuous cases have been compared [28], and the approach has been extended to curved surfaces [29].

In this paper, we consider when the sign of growth is switched in the DLA model, corresponding to dissolution or erosion: we start with a solid object, and then random walkers annihilate a small parts of it on contact. This case has received much less investigation, since it usually leads to stable dynamics [30, 31, 32] and thus many of the complex patterns due to growth instabilities are no longer manifest. However, this model opens up alternative questions for study. In a previous paper [33], several different conformally invariant transport-limited dissolution models were introduced, including the erosion of corrugations on an infinite surface, and the expansion of a cavity due to dissolution. The paper also introduced the system of advection–diffusion-limited dissolution (ADLD), whereby an object is dissolved due to a concentration of random walkers in a fluid flowing past the object. The object is represented by a time-dependent conformal map from the unit circle to the physical domain, described by a Laurent series. By making use of previous asymptotic results [27], an evolution equation for the conformal map is derived (Section 2).

The analysis of ADLD in this previous paper was entirely analytical, and thus only considered the simple shapes of a circle and ellipse, which can be described by three Laurent coefficients. Here, we investigate this model in more depth, and develop a numerical implementation that can simulate the dissolution of arbitrarily shaped objects. Starting from the evolution equation, a system of ordinary differential equations is derived that govern how the Laurent series coefficients evolve with time (Section 3). We numerically integrate this system using eighth-order timestepping [34, 35], which allows the dissolution process to be simulated very accurately, close to the limit of machine precision.

Our initial numerical results for a variety of objects show that they completely dissolve in a finite duration with their boundaries becoming progressively smoother (Section 4). As expected, the flow causes the objects to dissolve more quickly on the side facing upstream, although the details of the process are complicated, and affected by the precise manner that the fluid flows past the dissolving object. Of particular interest is the location of the collapse point, where the dissolving object finally vanishes. Due to the high accuracy of our simulations, we inferred an exact relationship between the collapse point z_c expressed as a complex number, the speed of the flow, and the initial Laurent coefficients. The relationship is surprising, whereby z_c is the root of a non-analytic function P , the terms of which involve complicated products of Laurent series terms. While some of these terms

share similarities with binomial and multinomial expansions, they are distinctly different, and we are unaware of any other problem in conformal mapping or elsewhere where they occur.

In Section 5 we make use of residue calculus to derive the general form of P , using the numerical results as a guide. The complicated products of terms in P arise from the residue of a contour integral where several Laurent series are multiplied together. In general, the function P has multiple roots, thus creating ambiguity about which root is the collapse point, and in Section 6 we consider three different example objects that highlight the structure of P in more detail. To find the roots of P , we introduce a modified Newton–Raphson iteration. As usual for Newton–Raphson iterations, plots of the root convergence in terms of the initial starting guess are fractal, but the non-analyticity of P creates some distinct morphological differences, and the plots illustrate the difficulties of determining the collapse point with mathematical certainty. While the dissolution model that we consider is a simplified model with stable dynamics, it has a surprising degree of mathematical structure, and our results raise a number of questions for further study.

2. Theoretical background

We make use of non-dimensionalized units, and consider an object in two dimensions with a time-dependent boundary $S(t)$ as shown in Fig. 1(a). The object is immersed in an inviscid, irrotational fluid with velocity $\mathbf{v}(\mathbf{x}, t)$, which can be written in terms of a potential $\phi(\mathbf{x}, t)$ as $\mathbf{v} = \nabla\phi$. The fluid is incompressible, so $\nabla \cdot \mathbf{v} = 0$ and hence

$$\nabla^2\phi = 0. \quad (1)$$

At the boundary of the object the condition $\hat{\mathbf{n}} \cdot \mathbf{v} = \hat{\mathbf{n}} \cdot \nabla\phi = 0$ is used, where $\hat{\mathbf{n}}$ is an outward-pointing normal vector. Far away from the object the flow tends to a constant horizontal velocity so that $\mathbf{v}(\mathbf{x}, t) \rightarrow (1, 0)$ as $|\mathbf{x}| \rightarrow \infty$. Equivalently, the potential satisfies $\phi(\mathbf{x}, t) \rightarrow x$ as $|\mathbf{x}| \rightarrow \infty$.

The fluid transports a random walker concentration $c(\mathbf{x}, t)$ that satisfies the advection–diffusion equation

$$\text{Pe} \nabla c \cdot \nabla\phi = \nabla^2 c, \quad (2)$$

where Pe is the Péclet number, a dimensionless quantity describing the ratio of advection to diffusion. Far away from the object, the random walker concentration tends to unity, so that $c(\mathbf{x}, t) \rightarrow 1$ as $|\mathbf{x}| \rightarrow \infty$. The random walkers are responsible for dissolving the object. At the boundary of the object, $c(\mathbf{x}, 0) = 0$. The normal velocity of the object boundary $S(t)$ is given by

$$\sigma = -\lambda \hat{\mathbf{n}} \cdot \nabla c, \quad (3)$$

where λ is a dimensionless constant. Equations 1 and 2 together with the associated boundary conditions form a closed system for (ϕ, c, S) that describe the dissolution dynamics, but they are difficult to solve directly. To proceed, we therefore treat the object as being in the complex z plane, where $z = x + iy$, and we introduce a time-dependent conformal map described by an analytic function $z = g(w, t)$ that transforms the unit circle C into the object boundary $S(t)$, as shown in Figure 1(b). The most general form of the conformal map is the truncated Laurent series,

$$g(w, t) = a(t)w + \sum_{n=0}^N q_n(t)w^{-n}, \quad (4)$$

where $a(t)$ is taken to be a real function, and $q_n(t)$ are complex functions. Hereafter, we refer to q_n as the n th mode. Both Eqs. 1 and 2 are conformally invariant. The Laplacian is the standard example of a conformally invariant operator, and the advective term $\nabla c \cdot \nabla \phi$ is also conformally invariant [25, 26].

The boundary conditions in the w plane are different. Due to the scaling factor $a(t)$ in Eq. 4, the boundary condition on the velocity potential becomes $\phi(w, t) \rightarrow a \operatorname{Re}(w)$ as $|w| \rightarrow \infty$. We therefore introduce a rescaled potential $\hat{\phi}(w, t) = \phi(w, t)/a$ that satisfies the original boundary condition $\hat{\phi}(w, t) \rightarrow \operatorname{Re}(w)$ as $|w| \rightarrow \infty$. The rescaled system for c and $\hat{\phi}$ satisfies Eqs. 1 & 2, but with a rescaled Péclet number $\tilde{\text{Pe}}(t) = \text{Pe } a(t)$. In addition, the normal growth in the w plane is $\sigma_w = \sigma/|g'|$ to take into account the local volumetric scaling of the conformal map.

Even in the w plane where the object is the unit circle, the concentration c cannot be determined analytically. However, asymptotic expansions have been studied in detail [27], and for Péclet numbers below 0.1, the approximation

$$\sigma_w \sim \frac{\lambda I_0(\tilde{\text{Pe}}) e^{\tilde{\text{Pe}} \cos \theta}}{K_0\left(\frac{\tilde{\text{Pe}}}{2}\right)} - \lambda \tilde{\text{Pe}} \left(\cos \theta + \int_0^{\tilde{\text{Pe}}} \frac{I_1(t) e^{t \cos \theta}}{t} dt \right), \quad (5)$$

is uniformly accurate in $\theta = \arg w$. Taking the leading term of this approximation gives

$$\sigma_w \sim \frac{\lambda(1 + \tilde{\text{Pe}} \cos \theta)}{-\gamma - \log \frac{\tilde{\text{Pe}}}{4}} - \lambda \tilde{\text{Pe}} \cos \theta, \quad (6)$$

where γ is Euler's constant.

To make progress, we now focus on the intermediate regime starting at small Péclet number and ending prior to collapse, in which it is reasonable to assume that $\log \tilde{\text{Pe}}$ is a constant. By rescaling the time, we choose $\lambda = \gamma + \log \frac{\tilde{\text{Pe}}}{4}$ without loss of generality. If the constant $B = \text{Pe} \lambda$ is introduced, which we subsequently refer to as the flow strength, then Eq. 6 becomes

$$\sigma_w = -1 + B a(t) \cos \theta. \quad (7)$$

To transform this back into the physical domain, consider a point on the $z(t) = g(w(t), t)$ on the boundary $S(t)$ of the object. Taking a time derivative gives $\dot{z} = g' \dot{w} + \dot{g}$. Multiplying by $\overline{w g'}$ and taking the real part gives

$$\operatorname{Re}(\overline{w g'} \dot{z}) = \operatorname{Re}(\overline{w g'} g' \dot{w}) + \operatorname{Re}(\overline{w g'} \dot{g}). \quad (8)$$

Since the point in the w plane mapping to $z(t)$ must lie on the unit circle, it follows that $w \bar{w} = 1$ and hence $\operatorname{Re}(\bar{w} \dot{w}) = 0$, so the first term on the right hand side of Eq. 8 vanishes. The motion of the point in the z plane is $\dot{z} = \sigma \hat{n}$ where \hat{n} is the normal vector written as a complex number. Taking into account rotation and scaling, the normal vector is given by

$$\hat{n} = \frac{g'}{|g'|} \frac{w}{|w|} \quad (9)$$

and hence the left hand side of Eq. 8 is

$$\operatorname{Re}(\overline{w g'} \dot{z}) = \operatorname{Re} \left(\frac{\overline{w g'} g' w \sigma}{|g' w|} \right) = \operatorname{Re}(|g'| \sigma) = \sigma_w. \quad (10)$$

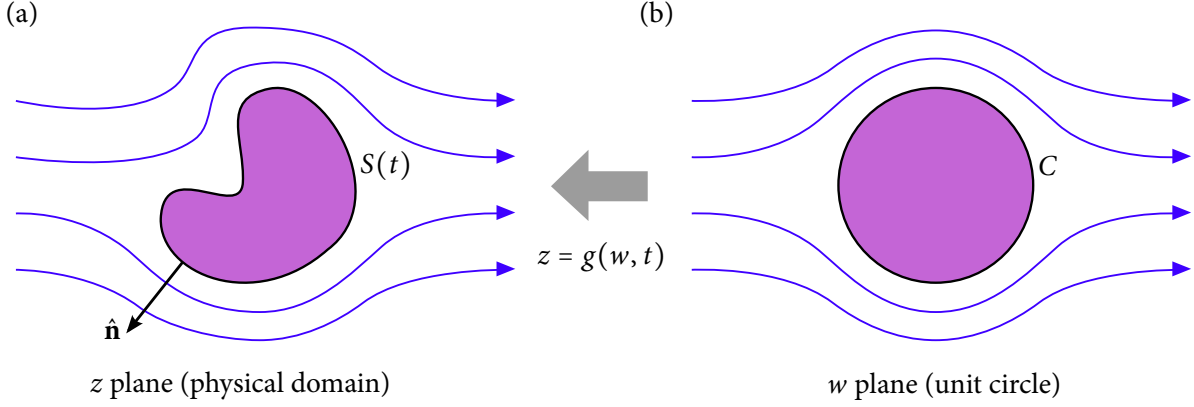


Figure 1: (a) The physical problem considered, where a two-dimensional object with time-dependent boundary $S(t)$ is dissolved a chemical concentration being transported by an incompressible potential flow. (b) A reference domain of the same physical problem but where the boundary is the unit circle C . A time-dependent conformal map $z = g(w, t)$ describes the transformation between the two domains.

Combining Eqs. 7, 8, and 10 yields

$$\text{Re}(\overline{w}g'\dot{g}) = -1 + Ba(t) \cos \theta, \quad (11)$$

which describes the dissolution process in terms of a time-dependent conformal map. For $B = 0$ it becomes the Polubarinova–Galín equation, which has been used in previous continuum DLA studies without advection [17, 19]. Here, the incorporation of the $Ba(t) \cos \theta$ term represents the simplest extension to account for the fluid flow and is therefore a useful model to study in its own right.

3. Numerical method and implementation

3.1. Discrete formulation of the governing equation

We now make use of Eq. 11 to formulate a numerical solution technique. We represent the dissolving object via the time-dependent conformal map in Eq. 4 with a fixed value of $N \geq 1$. We write the $q_n(t)$ in component form as $b_n(t) + ic_n(t)$, and describe the shape of the object by the real vector $\mathbf{s}(t) = (a, b_0, b_1, \dots, b_N, c_0, c_1, \dots, c_N)$, with a total of $2N + 3$ components. Using the two expressions

$$\overline{w}g' = a\bar{w} - \sum_{n=0}^N n(b_n - ic_n)\bar{w}^{-n}, \quad \dot{g} = \dot{a} + \sum_{n=0}^N (\dot{b}_n + i\dot{c}_n)w^{-n}, \quad (12)$$

Eq. 11 becomes

$$-1 + Ba \cos \theta = \text{Re} \left(\left[ae^{-i\theta} - \sum_{n=0}^N n(b_n - ic_n)e^{in\theta} \right] \left[\dot{a}e^{i\theta} + \sum_{n=0}^N (\dot{b}_n + i\dot{c}_n)e^{-in\theta} \right] \right). \quad (13)$$

Eq. 13 is real, and can be expressed in terms of components $\cos n\theta$ and $\sin n\theta$ for $n = 1, \dots, N + 1$, plus a constant term. Equating both sides of the Eq. 13 in each component leads to $2N + 3$ coupled ordinary differential equations for the $2N + 3$ variables $a(t)$, $b_n(t)$, and $c_n(t)$. Hence, other than for cases where these equations are degenerate, $\dot{\mathbf{s}}$ will be uniquely determined in terms of \mathbf{s} . Furthermore,

since Eq. 13 does not feature any higher harmonic of sine and cosine, it follows \mathbf{s} exactly represents the time-evolution prescribed by Eq. 11; if a shape initially is described in terms of a Laurent series using terms up to q_N , it will remain perfectly described by this Laurent series throughout the whole dissolution process.

The details of equating each component of Eq. 13 are given in Appendix A. Equating the constant terms gives

$$a\dot{a} - \sum_{n=0}^N n(b_n\dot{b}_n + c_n\dot{c}_n) = -1. \quad (14)$$

Equating the terms with factors $\cos(N+1)\theta$ and $\sin(N+1)\theta$ gives

$$a\dot{b}_N = \dot{a}Nb_N, \quad a\dot{c}_N = \dot{a}Nc_N, \quad (15)$$

respectively. Equating the terms with a factor of $\sin n\theta$ for $n = 1, \dots, N$ gives

$$-\dot{a}(n-1)c_{n-1} + a\dot{c}_{n-1} - \sum_{m=0}^{N-n} \left[(m+n)(c_{m+n}\dot{b}_m - b_{m+n}\dot{c}_m) - m(c_m\dot{b}_{m+n} - b_m\dot{c}_{m+n}) \right] = 0. \quad (16)$$

Finally, equating the terms with a factor of $\cos n\theta$ for $n = 1, \dots, N$ gives

$$-\dot{a}(n-1)b_{n-1} + a\dot{b}_{n-1} - \sum_{m=0}^{N-n} \left[(m+n)(b_{m+n}\dot{b}_m + c_{m+n}\dot{c}_m) + m(b_m\dot{b}_{m+n} + c_m\dot{c}_{m+n}) \right] = \beta_n \quad (17)$$

where $\beta_n = Ba$ if $n = 1$, and $\beta_n = 0$ otherwise. The combination of Eqs. 14, 15, 16, and 17 can then be expressed as a linear system

$$M(\mathbf{s})\dot{\mathbf{s}} = \mathbf{v}(\mathbf{s}) \quad (18)$$

where M and \mathbf{v} are matrix and vector functions of \mathbf{s} , respectively. By writing Eq. 18 as $\dot{\mathbf{s}} = M^{-1}(\mathbf{s})\mathbf{v}(\mathbf{s})$, the system can be integrated numerically.

3.2. Numerical implementation

The simulations are carried out using double-precision floating point arithmetic, using LAPACK [36] to invert the linear system in Eq. 18. To time-integrate the equation, the DOP853 integration routine described by Hairer *et al.* [34] is used. This routine uses the eighth-order, thirteen-step Dormand–Prince integration method that has the first-same-as-last (FSAL) property, requiring twelve function evaluations per timestep [37]. As described in more detail later, the components of \mathbf{s} can sometimes vary rapidly, particularly close to the time of collapse. The DOP853 routine employs adaptive timestepping, which can retain accuracy in this situation. The routine estimates the local error¹ using a combination of fifth-order and third-order embedded numerical schemes. For all of the subsequent results, the timestep size Δt is continually adjusted so that the absolute local error per timestep remains below a tolerance of 10^{-14} . If the estimated error of a timestep exceeds the tolerance, then the timestep is rejected and the integrator tries again with a reduced Δt .

¹The local error is defined as $(\sum_{i=1}^{2N+3} e_i^2)^{1/2}$ where e_i is the estimated error of the i th component of \mathbf{s} during a single timestep.

There are three scenarios where the DOP853 integrator terminates early: (i) if a maximum number of timesteps is reached, (ii) if the equations are detected as stiff [35], or (iii) if the timestep Δt required achieve the desired local error becomes too small. In the following results, we have only observed the third scenario. Specifically, this occurs when Δt becomes smaller than $10u_r t$, where $u_r = 2.3 \times 10^{-16}$ is an estimate of the smallest number satisfying $1.0 + u_r > 1.0$ in double-precision floating point arithmetic. In certain cases, such as the examples of Subsecs. 6.1 and 6.3, the third scenario signifies a breakdown of the physical problem due to the formation of a cusp. However, the third scenario also occurs in many normal cases close to the time of collapse t_c due to $a(t)$ varying rapidly. If the DOP853 integrator terminates within $10^4 u_r$ of t_c then we manually advance to t_c using timesteps of $10u_r$ or less. While this may no longer achieve the required level of local error, we find that it provides several additional digits of accuracy in the collapse point location, which is important in some of the later analysis.

In some of the subsequent results, we need to evaluate \mathbf{s} at time points spaced at fixed intervals, which may not precisely coincide with the time points that are selected during the adaptive time-integration, which are usually unevenly spaced. To solve this we make use of the dense output formulae described by Hairer *et al.* [34]. By doing three additional integration steps, a seventh-order accurate interpolation formula over the interval of a timestep can be calculated, allowing \mathbf{s} to be evaluated at any specific time point. For computational efficiency, these three additional steps are only done when one or more output time points overlaps with the current timestep interval.

The simulations are implemented in C++, and the code required to carry out all of the subsequent analysis is provided as Supplementary Information. For all of the results presented here, the computation time required to simulate the dissolution process is negligible, taking less than 0.25 s on a Mac Pro (Late 2013) with an 8-core 3GHz Intel Xeon E5 processor.

4. Results

4.1. Analytic results for the area and highest mode amplitude

Before presenting results of the numerical method, it is useful to establish some basic features of the equations presented in the previous section. The area of the object is given by the integral

$$A(t) = \iint_{\Omega} dz \quad (19)$$

where Ω is the region enclosed by $S(t)$. Using Green's identity in complex form,

$$A(t) = -\frac{1}{2i} \oint_{S(t)} z d\bar{z} = \frac{1}{2i} \int_C g(w) \overline{g'(w)} d\bar{w}. \quad (20)$$

Since $w\bar{w} = 1$ on the unit circle, the integrand can be converted into an analytic function,

$$A(t) = \frac{1}{2i} \int_C g(w) \overline{g'(w)} \frac{dw}{w^2} = \frac{1}{2i} \int_C \left(a - \sum_{n=0}^N q_n n w^{-(n+1)} \right) \left(\frac{a}{w} + \sum_{n=0}^N \bar{q}_n w^n \right) dw \quad (21)$$

and applying residue calculus gives,

$$A(t) = \pi \left(a^2 - \sum_{n=0}^N n |q_n|^2 \right) = \pi \left(a^2 - \sum_{n=0}^N n (b_n^2 + c_n^2) \right), \quad (22)$$

describing the area as a function of the current mode amplitudes. Furthermore, time-integrating Eq. 14 gives

$$a^2 - \sum_{n=0}^N n(b_n^2 + c_n^2) = C - 2t, \quad (23)$$

where C is a constant, and hence

$$A(t) = A_0 - 2\pi t, \quad (24)$$

where A_0 is the initial area of the object. The area of the object therefore decreases at a constant rate, independent of the flow parameter B , with the time to collapse given by

$$t_c = \frac{A_0}{2\pi} = \frac{1}{2} \left(a^2 - \sum_{n=0}^N n|q_n|^2 \right). \quad (25)$$

The modes in Eq. 15 also have first integrals,

$$b_N = ka^N, \quad c_N = la^N \quad (26)$$

for some constants k and l . The highest mode amplitudes are therefore only dependent on the conformal radius a . Due to the couplings in Eqs. 16 and 17, similar results for the lower modes do not exist.

4.2. Initial numerical results

Figure 2 shows the dissolution process for six objects calculated using the numerical code, where for all cases $a(0) = 1$ and $B = 0.7$. Figure 2(a) shows the dissolution process for a circle. Throughout the process, the circle retains its shape although its center progressively moves rightward due to the effect of the flow, which preferentially dissolves the side of the circle facing upstream. A similar behavior is visible in Fig. 2(b) for an ellipse, which keeps its shape through the dissolution process, while the ellipse center moves up and right. The results for Figs. 2(a) and 2(b) match those that were previously studied analytically [33].

Figure 2(c) shows the dissolution process for a triangular-shaped object given by setting $q_2 = -0.35$ initially. In general, the mode q_n is responsible for an $(n + 1)$ -fold perturbation of the boundary. If all of the q_n are initially real, the object is symmetric about the x axis, and will remain symmetric throughout the dissolution process. For the case shown, the point of the triangle that faces upstream is more rapidly dissolved than the other two. Unlike the previous two examples that retain their shape during dissolution, the triangle becomes progressively more rounded at later times. Figure 2(d) shows the dissolution process when the previous object is rotated by 90° , which is achieved by setting $q_2 = 0.35i$. This object is initially symmetric about the y axis, but the flow causes this symmetry to be lost as time passes. The collapse point is slightly up and right from the origin.

Figure 2(e) shows the dissolution process for the case when $q_{15} = 0.05i$ initially, which creates a 16-fold perturbation in the boundary. After 20% of the object has dissolved, this perturbation is almost completely removed, with the object's shape approaching that of a circle. This is expected from Eq. 26, which shows that the highest mode will be proportional a^N and hence decay more rapidly for larger N . If several modes are initially non-zero as in Fig. 2(f) an irregular shape is formed,

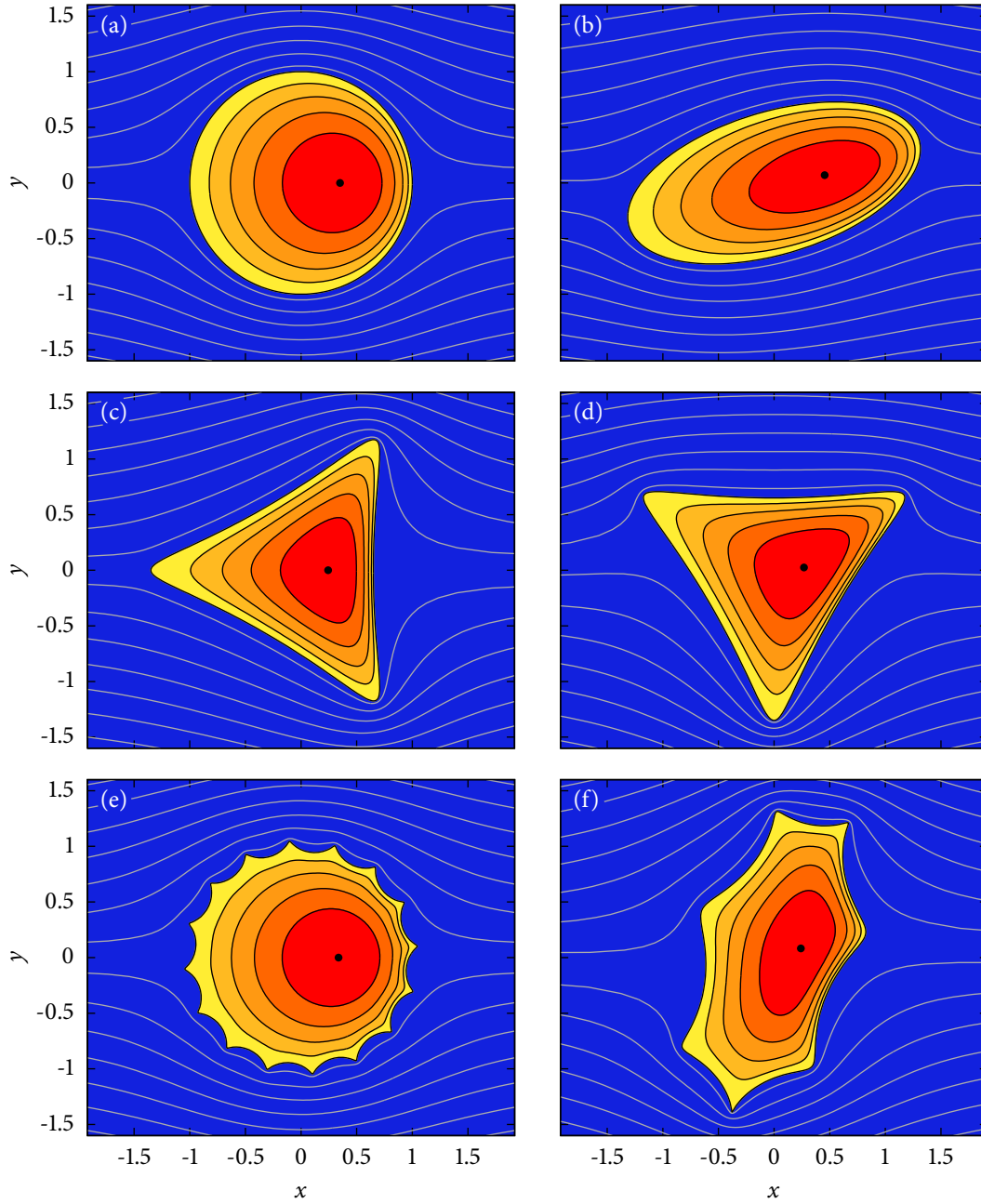


Figure 2: Sample dissolution processes for six objects, all starting with $a = 1$ and using $B = 0.7$. The six objects and initial non-zero modes are (a) a circle, (b) an ellipse with $q_1 = 0.3 + 0.2i$, (c) a triangle with $q_2 = -0.35$, (d) a triangle with $q_2 = 0.35i$, (e) a corrugated circle with $q_{15} = 0.05i$, and (f) an irregular object with $q_1 = -0.28 + 0.2i$ and $q_6 = 0.1$. The white lines show the flow streamlines around the initial shape. The colored regions shown the shapes of the object at successive times as it dissolves, where each progressive region represents the dissolution of 20% of the object's initial area. The black circles indicate the final points of collapse.

which behaves like a combination of the previous examples, with sharp features in the boundary being rapidly removed.

We now examine the evolution of the modes and look in detail at the effect of the flow strength B . We make use of the specific example of a diamond shape given by $a = 1$ and $q_3 = 0.25$ initially. Figure 3(a) shows the dissolution process for the case of zero flow when $B = 0$. Similar to Figs. 2(c) and 2(d) the object becomes progressively more circular, but without the presence of flow it retains symmetry in the x axis, y axis, and the line $x = y$. Figure 3(b) shows the time-evolution of the modes throughout the dissolution process. The modes q_0, q_1, q_2 , which were zero initially, remain zero throughout the dissolution process—this is expected since any non-zero contribution from these modes would break at least one of the symmetries seen in Fig. 3(a). The dissolution process is therefore described entirely in terms of a and q_3 , and could therefore be determined analytically using Eqs. 23 and 26, as considered in previous work [17, 38, 33]. Since q_0 remains at zero, the collapse point is at the origin.

Figure 3(c) shows the dissolution of the diamond when the flow parameter is $B = 0.7$. As in the previous examples of Fig. 2, the diamond dissolves more rapidly on the side facing upstream, and the collapse point is slightly downstream. The time evolution of the modes (Fig. 3(d)) is significantly altered in this case, with all three components q_0, q_1 , and q_2 becoming non-zero during the dissolution process, due to the mixing between modes via the advection term in Eq. 11. The effects of these three modes, such as the translation of the object center, and the loss of symmetry about the y axis, are clearly visible in Fig. 3(c). The q_1 and q_2 modes decay to zero at the point of collapse, while the q_0 mode remains positive. The value of q_0 at $t = t_c$ gives the collapse point position.

Figures 3(b) and 3(d) also indicate the adaptive integration timesteps chosen by the DOP853 integration routine. In the middle of the dissolution process, at $t \approx 0.2$, the routine is able to take timesteps up to approximately 0.02 while retaining the desired level of local error of 10^{-14} . However, close to $t = t_c$, many more timesteps are needed to resolve the rapid change in a . For the example shown in Fig. 3(d), a total of 332 integration timesteps are evaluated. During the DOP853 integration routine, 199 steps are accepted, and 128 are rejected due to the local error estimate exceeding the given tolerance. Five additional small steps are required to reach the collapse time t_c .

4.3. Inferring analytic formulae for the collapse point

Figures 2 and 3 show that the collapse point $z_c = x_c + iy_c$ of the dissolution process is dependent on both the flow strength B and the initial shape of the body as described by its Laurent coefficients. Since there are no other quantities in the problem, z_c must be given in terms of B and the Laurent coefficients only. The precise form of this dependence is not obvious, as the collapse point is given as the component q_0 of the nonlinear differential equation system, evaluated at the time of collapse t_c .

In this section, we infer the exact form of this relationship by exploiting the very high accuracy of the simulations, which allow the collapse point to be calculated to at least twelve decimal places. To simplify the analysis, we set $a = 1$ throughout this section. To begin, we restrict to the case when the Laurent coefficients are given purely in terms of real components b_j . As discussed in the previous section, the components will remain real throughout the simulation, and the object will be symmetric about the x axis. Hence the collapse point z_c will be real, and determined entirely in terms of the horizontal position x_c .

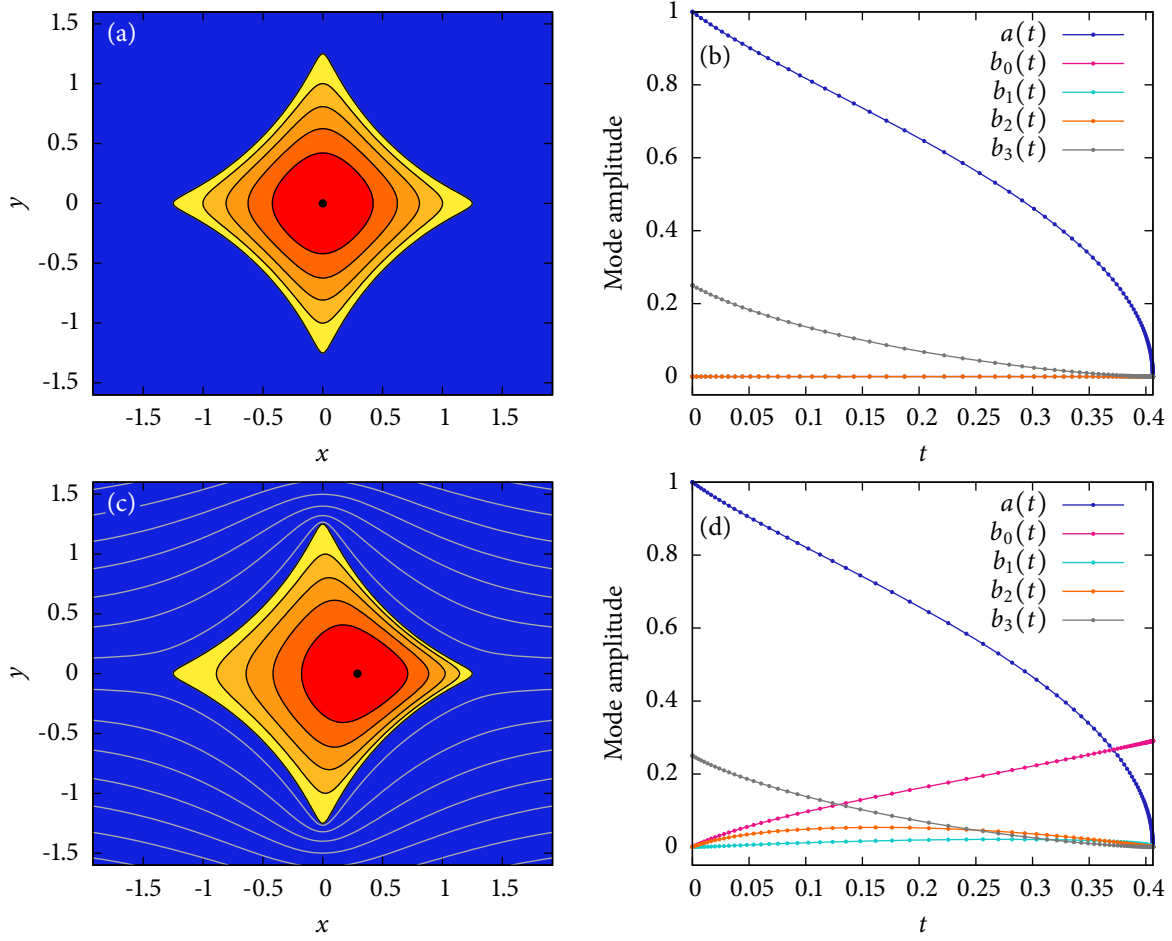


Figure 3: (a) Dissolution process of a diamond shape initially described by non-zero modes $a = 1$ and $q_3 = 0.25$ for the case of zero flow, $B = 0$. The colored regions shown the shapes of the object at successive times as it dissolves, where each progressive region represents the dissolution of 20% of the object's area, with the black circle indicating the point of collapse. (b) Time-evolution of the modes describing the diamond during dissolution, where the small circles on each curve show the integration timesteps using the adaptive DOP853 integration scheme. (c) Dissolution process of the diamond when the flow is $B = 0.7$. (d) Time-evolution of the modes describing the diamond during dissolution with flow, with the small circles on each curve showing the integration timesteps.

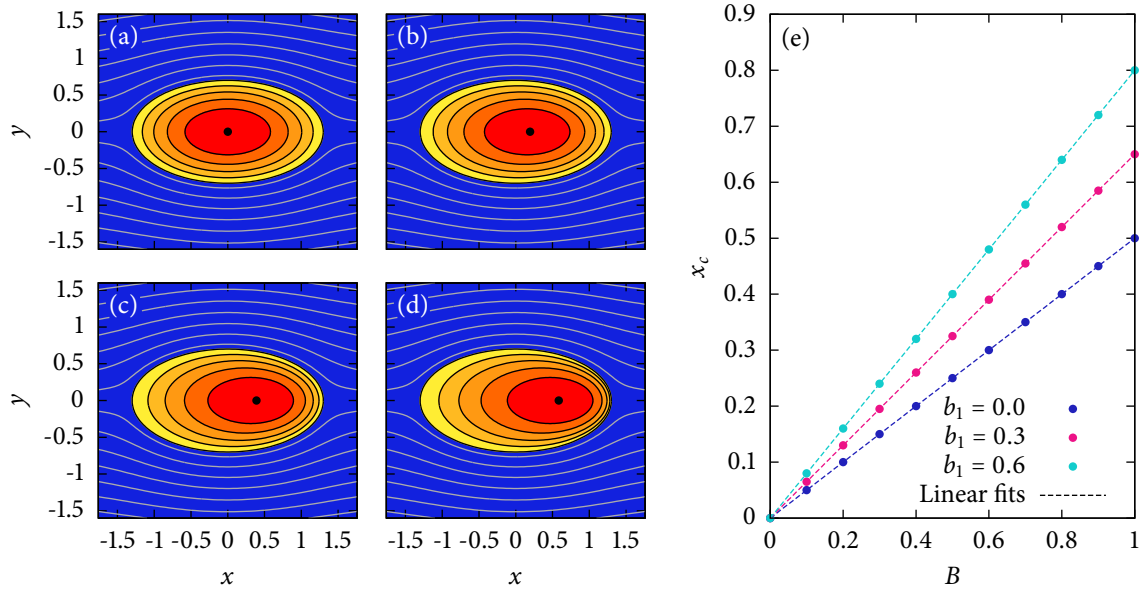


Figure 4: An example procedure to infer the analytic formula for position of collapse point in terms of the initial modes. (a–d) Dissolution processes of an ellipse given by $a = 1, q_1 = 0.3$ for flow speeds of $B = 0, 0.3, 0.6, 0.9$, respectively, using the same visual representation as described in Fig. 2. (e) Plot of the numerically computed horizontal collapse point position $x_c = \text{Re } z_c$ as a function of B for three different values of b_1 , which match linear relationships to numerical precision, suggesting an analytical relationship.

Figure 4 shows an example of inferring an analytic relationship, for the case of an ellipse where the only non-zero Laurent coefficient is b_1 . Figures 4(a–d) show four dissolution process are shown for when $b_1 = 0.3$ and the flow strength is $B = 0, 0.3, 0.6, 0.9$, respectively. The collapse point x_c moves progressively right as B is increased. In Fig. 4(e), the numerically computed x_c is plotted as a function of B , for three different values of b_1 of 0.0, 0.3, and 0.6. The plot demonstrates that x_c is linear in B , with the slope depending on b_1 . The numerical data matches the relationship

$$x_c = \frac{B(1 + b_1)}{2}, \quad (27)$$

with the sum of square residuals being 1.4×10^{-30} , 1.5×10^{-30} , and 2.6×10^{-30} for $b_1 = 0, 0.3, 0.6$, respectively. These small residuals, which are of a similar size to the expected numerical error, strongly suggest that this is an exact relationship for the original mathematical problem.

One can extend this analysis to the case where the only non-zero Laurent coefficient is b_n , and determine that x_c satisfies the polynomial relationship

$$\frac{B}{2} = \frac{x_c - b_n x_c^n}{1 - n b_n^2 x_c^{n-1}}. \quad (28)$$

For $n = 1$, this is consistent with Eq. 27 for the ellipse, although it also reveals more structure, and by substituting Eq. 25 the relationship simplifies to

$$B t_c = x_c - b_n x_c^n. \quad (29)$$

n	$Q(x_c)$
2	$-b_2x_c^2 + 2b_2b_1 + (1-b_1)x_c$
3	$-b_3x_c^3 + 3b_3b_1x_c + (1-b_1)x_c$
4	$-b_4x_c^4 + 4b_4b_1x_c^2 - 2b_4b_1^2 + (1-b_1)x_c$
5	$-b_5x_c^5 + 5b_5b_1x_c^3 - 5b_5b_1^2)x_c + (1-b_1)x_c$
6	$-b_6x_c^6 + 6b_6b_1x_c^4 - 9b_6b_1^2x_c^2 + 2b_6b_1^3 + (1-b_1)x_c$
7	$-b_7x_c^7 + 7b_7b_1x_c^5 - 14b_7b_1^2x_c^3 + 7b_7b_1^3x_c + (1-b_1)x_c$
8	$-b_8x_c^8 + 8b_8b_1x_c^6 - 20b_8b_1^2x_c^4 + 16b_8b_1^3x_c^2 - 2b_8b_1^4 + (1-b_1)x_c$
9	$-b_9x_c^9 + 9b_9b_1x_c^7 - 27b_9b_1^2x_c^5 + 30b_9b_1^3x_c^3 + 9b_9b_1^4x_c + (1-b_1)x_c$
10	$-b_{10}x_c^{10} + 10b_{10}b_1x_c^8 - 35b_{10}b_1^2x_c^6 + 50b_{10}b_1^3x_c^4 - 25b_{10}b_1^4x_c^2 + 2b_{10}b_1^5 + (1-b_1)x_c$
	$-b_nx_c^n + nb_nb_1x_c^{n-2} - \frac{n(n-3)}{2}b_nb_1^2x_c^{n-4} + \frac{n(n-4)(n-5)}{6}b_nb_1^3x_c^{n-6} - \dots + (1-b_1)x_c$

Table 1: Examples of the analytic relationship $Bt_c = Q(x_c)$ for the horizontal collapse point position x_c that were inferred numerically using the high-precision calculations, for the case of an object described by two real non-zero Laurent coefficients b_1 and b_n . The integer coefficients colored in blue, green, and red follow patterns. The final line of the table shows an inferred general formula.

To proceed, we now consider if there are two non-zero Laurent coefficients. The simplest case would be b_0 and b_n being non-zero, for $n \geq 1$. Since b_0 corresponds to a translation, the relationship is immediately given by

$$Bt_c = (x_c - b_0) - b_n(x_c - b_0)^n, \quad (30)$$

without the need for simulation. Expanding the second term yields

$$Bt_c = -b_nx_c^n + nb_nb_0x_c^{n-1} - \frac{n(n-1)}{2}b_nb_0^2x_c^{n-2} + \frac{n(n-1)(n-2)}{6}b_nb_0^3x_c^{n-3} - \dots + (x_c - b_0) \quad (31)$$

where the coefficients on the powers of x_c follow Pascal's triangle.

The next case to consider is when b_1 and b_n are non-zero, for $n \geq 2$. Unlike the previous case this cannot be immediately derived, and must be inferred through fitting to simulation. Table 1 shows the derived results for the cases of $n = 2, 3, \dots, 10$ where a surprising pattern emerges. We see polynomials that bear some resemblance to a binomial expansion, although in contrast to Eq. 31, only every second power of x_c is present. Furthermore, the coefficients in front of the terms are integer, but of a more complicated form than Pascal's triangle. Unlike the previous case, the more complicated form of these polynomials precludes rewriting them in a succinct form like Eq. 30. The pattern continues for the case when b_2 and b_n are non-zero, for $n \geq 3$. As shown in Table 2, only every third power of x_c is present. The integer coefficients follow a natural progression from those in Table 1.

In Tables 1 and 2, we observe that each pair of non-zero Laurent coefficients leads to a combination of additional terms appearing in the collapse point polynomial. Building on these results, we inferred and numerically tested the formula

$$Bt_c = -b_4x_c^4 - x_c^3 + x_c^2(4b_4b_1 - b_2) + x_c(1 - b_1 + 3b_3b_1 + 4b_4b_2) + 2b_2b_1 + 3b_3b_2 + 4b_4b_3 - 2b_4b_1^2 \quad (32)$$

n	$Q(x_c)$
3	$-b_3x_c^3 + 3b_3b_2 + (x_c - b_2x_c^2)$
4	$-b_4x_c^4 + 4b_4b_2x_c + (x_c - b_2x_c^2)$
5	$-b_5x_c^5 + 5b_5b_2x_c^2 + (x_c - b_2x_c^2)$
6	$-b_6x_c^6 + 6b_6b_2x_c^3 - 3b_6b_2^2 + (x_c - b_2x_c^2)$
7	$-b_7x_c^7 + 7b_7b_2x_c^4 - 7b_7b_2^2x_c + (x_c - b_2x_c^2)$
8	$-b_8x_c^8 + 8b_8b_2x_c^5 - 12b_8b_2^2x_c^2 + (x_c - b_2x_c^2)$
9	$-b_9x_c^9 + 9b_9b_2x_c^6 - 18b_9b_2^2x_c^3 + 3b_9b_1^3 + (x_c - b_2x_c^2)$
10	$-b_{10}x_c^{10} + 10b_{10}b_2x_c^7 - 25b_{10}b_2^2x_c^4 + 10b_{10}b_2^3x_c + (x_c - b_2x_c^2)$
11	$-b_{11}x_c^{11} + 11b_{11}b_2x_c^8 - 33b_{11}b_2^2x_c^5 + 22b_{11}b_2^3x_c^2 + (x_c - b_2x_c^2)$
12	$-b_{12}x_c^{12} + 12b_{12}b_2x_c^9 - 42b_{12}b_2^2x_c^6 + 40b_{12}b_2^3x_c^3 - 3b_{12}b_2^4 + (x_c - b_2x_c^2)$
	$-b_nx_c^n + nb_nb_2x_c^{n-3} - \frac{n(n-5)}{2}b_nb_2^2x_c^{n-6} + \frac{n(n-7)(n-8)}{6}b_nb_2^3x_c^{n-9} - \dots + (x_c - b_2x_c^2)$

Table 2: Examples of the analytic relationship $Bt_c = Q(x_c)$ for the horizontal collapse point position x_c that were inferred numerically using the high-precision calculations, for the case of an object described by two real non-zero Laurent coefficients b_2 and b_n . The integer coefficients colored in blue, green, and red follow patterns. The final line of the table shows an inferred general formula.

for the case of all four coefficients b_1 , b_2 , b_3 , and b_4 being non-zero. In Eq. 32 all terms involve powers of two different b_n , but for higher non-zero Laurent coefficients, terms with three or more different b_n arise. If b_1 , b_2 , and b_5 are non-zero, then we find that

$$Bt_c = -b_5x_c^5 + 5b_5b_1x_c^3 + (5b_5b_2 - b_2)x_c^2 + (1 - b_1 - 5b_5b_1^2) + 2b_2b_1 - 4b_5b_2b_1, \quad (33)$$

where the last term on the right hand side is a product of all three non-zero Laurent coefficients.

The final generalization that we consider is when the Laurent coefficients are complex. The fitting procedure described in Fig. 4 becomes more complicated in this case, since both the horizontal position x_c and the vertical position y_c of the collapse point will vary. For the case of the Laurent coefficients q_1 and q_4 being non-zero and complex, we inferred the formula

$$Bt_c = \bar{z}_c - \bar{q}_1z_c - \bar{q}_4z_c^4 + 4\bar{q}_4q_1z_c^2 - 2\bar{q}_4q_1^2, \quad (34)$$

which is a generalization of the formula for $n = 4$ in Table 1. The generalization to complex coefficients introduces conjugates on some terms, and the right hand side is not an analytic function of z_c due to the first term featuring \bar{z}_c . If $q_4 = 0$ also, then Eq. 34 simplifies to

$$\frac{B}{2} = \frac{\bar{z}_c - \bar{q}_1z_c}{1 - q_1\bar{q}_1}, \quad (35)$$

which is equivalent to the formula for an ellipse $z_c = \frac{B}{2}(1 + q_1)$ that was derived in previous work [33].

5. Derivation of the collapse point formulae

The previous section revealed a surprising and complicated connection between the collapse point, initial shape of the object, and the flow strength. Using these numerical results as a guide,

we now analytically derive this connection. While the formulae in Tables 1 and 2 are complicated, it is reasonable to imagine that the specific coefficients could occur as the residue from a contour integral, perhaps involving the product of several Laurent series, and thus our first step is to consider a general integral quantity and determine its behavior during the dissolution process.

5.1. Time-evolution of an integral quantity

Consider the expression

$$I(t) = \oint_{S(t)} F(z) d\bar{z} \quad (36)$$

where $z = g(w)$, $S(t)$ is the shape of the object, and F is an arbitrary analytic function. This can be written as

$$I(t) = \oint_C F(g(w)) \overline{g'(w)} d\bar{w}, \quad (37)$$

where C is the unit circle, and $w = e^{i\theta}$. Since $\bar{w}w = 1$ on the unit circle, this can be converted into the integral of an analytic function,

$$I(t) = - \oint_C F(g(w)) \bar{g}'\left(\frac{1}{w}\right) \frac{dw}{w^2}, \quad (38)$$

which can be written as

$$I(t) = \oint_C F(g(w)) \frac{d}{dw} \left(\bar{g}\left(\frac{1}{w}\right) \right) dw \quad (39)$$

and hence integration by parts can be used to obtain

$$I(t) = - \oint_C F'(g(w)) g'(w) \bar{g}\left(\frac{1}{w}\right) dw. \quad (40)$$

This is the first of two expressions that will be used later. To obtain a second integral expression, consider taking the time derivative, which gives

$$\frac{dI}{dt} = - \oint_C \frac{d}{dw} \left(F'(g(w)) \right) \dot{g}(w) \bar{g}\left(\frac{1}{w}\right) dw - \oint_C F'(g(w)) \left(\dot{g}'(w) \bar{g}\left(\frac{1}{w}\right) + g'(w) \dot{\bar{g}}\left(\frac{1}{w}\right) \right) dw. \quad (41)$$

Integration by parts can be applied to the first integral, which will transfer the derivative onto the $\dot{g}(w) \bar{g}(1/w)$ terms. Note that

$$\frac{d}{dw} \left(\dot{g}(w) \bar{g}\left(\frac{1}{w}\right) \right) = \dot{g}'(w) \bar{g}\left(\frac{1}{w}\right) - \frac{\dot{g}(w)}{w^2} \bar{g}'\left(\frac{1}{w}\right) \quad (42)$$

and since the first term of this expression will cancel with one of the terms in second integral of Eq. 41, it follows that

$$\frac{dI}{dt} = - \oint_C F'(g(w)) \left(\frac{\dot{g}(w)}{w^2} \bar{g}'\left(\frac{1}{w}\right) + g'(w) \dot{\bar{g}}\left(\frac{1}{w}\right) \right) dw. \quad (43)$$

By substituting $w = e^{i\theta}$ and making use of Eq. 11,

$$\begin{aligned}
\frac{dI}{dt} &= - \int_0^{2\pi} F'(g(e^{i\theta})) i \left(\dot{g}(e^{i\theta}) \overline{g'(e^{i\theta})} e^{-i\theta} + g'(e^{i\theta}) \overline{\dot{g}(e^{i\theta})} e^{i\theta} \right) d\theta \\
&= -2i \int_0^{2\pi} F'(g(e^{i\theta})) \operatorname{Re} \left(\overline{g'(e^{i\theta})} e^{i\theta} \dot{g}(e^{i\theta}) \right) d\theta \\
&= 2i \int_0^{2\pi} F'(g(e^{i\theta})) (1 - Ba \cos \theta) d\theta.
\end{aligned} \tag{44}$$

This can be written as a contour integral as

$$\begin{aligned}
\frac{dI}{dt} &= i \int_0^{2\pi} F'(g(e^{i\theta})) (2 - Ba e^{i\theta} - Ba e^{-i\theta}) d\theta \\
&= \oint_C \frac{F'(g(w)) (2w - Ba - Baw^2) dw}{w^2},
\end{aligned} \tag{45}$$

yielding the second integral expression that will be used later. As a check, it is useful to consider when $F'(z) = 1$, in which case the integral matches the one in Eq. 20 for the area of the object. Then

$$\frac{dI}{dt} = \oint_C \frac{(2w - Ba - Baw^2) dw}{w^2} = 2\pi i (2) = 4\pi i \tag{46}$$

and

$$I(t) = - \oint_C \left(a - \sum_{n=0}^N q_n n w^{-(n+1)} \right) \left(\frac{a}{w} + \sum_{n=0}^N \bar{q}_n w^n \right) dw = -2\pi i \left(a^2 - \sum_{n=0}^N n |q_n|^2 \right) = -2\pi i A(t) \tag{47}$$

This gives $\dot{A}(t) = -2$, which agrees with Eq. 23.

5.2. A specific integral quantity

A interesting candidate for the function F' is

$$F'(z) = \frac{1}{z - z_c} \tag{48}$$

where z_c is the collapse point. This function is particularly special, since as the object is dissolving, the integrals given in Eqs. 40 and 45 will always be finite, as the integration contour will never pass over the singularity. Even though the function $F(z) = \log(z - z_c)$ is multivalued, the two integral expressions that will be used in the following derivation, Eqs. 40 and 45, are related to each other through a derivation only involving F' , and thus it is not necessary to consider branch cuts that would be needed to integrate F . Equation 45 will give

$$\frac{dI}{dt} = \oint_C \frac{(2w - Ba - Baw^2) dw}{w^2 (aw - z_c + \sum_{n=0}^N q_n w^{-n})} = \oint_C \frac{(2w - Ba - Baw^2) dw}{aw^3 \left(1 - \frac{1}{aw} \left(z_c - \sum_{n=0}^N q_n w^{-n} \right) \right)}. \tag{49}$$

Since $g(w, t)$ is a conformal map that takes the region $|w| \geq 1$ to the region outside the object, there can be no solutions to $g(w, t) = z_c$ for $|w| \geq 1$ and thus the above integrand will have no poles for

$|w| \geq 1$. Hence the integration contour can be deformed outwards and evaluated in terms of the residue at infinity, which is given by the coefficient of the w^{-1} term, namely $-Ba/a = -B$. Hence

$$\frac{dI}{dt} = -2\pi i B \quad (50)$$

and therefore $I(t) = D - 2\pi i B t$ for some constant D . To determine the constant, we consider the limit as $t \rightarrow t_c$, where $a \rightarrow 0$, $q_0 \rightarrow z_c$, and $q_n \rightarrow 0$ for all $n > 0$. Then Eq. 40 shows that

$$I(t) \rightarrow - \oint_C \frac{a \left(\frac{a}{w} + \bar{q}_0 \right) dw}{(aw - z_c + q_0)} = - \oint_C \frac{a \bar{q}_0}{aw} dw = -2\pi i \bar{z}_c \quad (51)$$

and therefore $I(t) = 2\pi i (B(t_c - t) - \bar{z}_c)$. Returning to Eq. 40, and examining the integral at the initial time,

$$I(0) = - \oint_C \frac{\left(a - \sum_{n=0}^N q_n n w^{-(n+1)} \right) \left(\frac{a}{w} + \sum_{n=0}^N \bar{q}_n w^n \right) dw}{aw - z_c + \sum_{n=0}^N q_n w^{-n}}, \quad (52)$$

which for large w can be expanded as

$$\begin{aligned} I(0) &= - \oint_C \frac{\left(a - \sum_{n=0}^N q_n n w^{-(n+1)} \right) \left(\frac{a}{w} + \sum_{n=0}^N \bar{q}_n w^n \right) dw}{(aw - z_c + \sum_{n=0}^N q_n w^{-n})} \\ &= - \oint_C \frac{\left(a - \sum_{n=0}^N q_n n w^{-(n+1)} \right) \left(\frac{a}{w} + \sum_{n=0}^N \bar{q}_n w^n \right) dw}{aw \left(1 - \frac{1}{aw} \left(z_c - \sum_{n=0}^N q_n w^{-n} \right) \right)} \\ &= - \oint_C \frac{1}{aw} \left(a - \sum_{n=0}^N \frac{n q_n}{w^{n+1}} \right) \left(\frac{a}{w} + \sum_{n=0}^N \bar{q}_n w^n \right) \left(\sum_{k=0}^{\infty} \frac{\left(z_c - \sum_{n=0}^N q_n w^{-n} \right)^k}{a^k w^k} \right) dw. \end{aligned} \quad (53)$$

While complicated, this integral will give the desired relationship between z_c and B . By expanding out the three power series, and looking at terms of the form w^{-1} that will give a residue at infinity, the integral will simplify to a polynomial in z_c . For example, consider the case of only q_1 and q_4 being non-zero. In that case, for w large, and neglecting terms smaller than w^{-1} ,

$$\begin{aligned} I(0) &= - \oint_C \left(\frac{1}{w} - \frac{q_1}{aw^3} - \frac{4q_4}{aw^6} \right) \left(\frac{a}{w} + \bar{q}_1 w + \bar{q}_4 w^4 \right) \left(\sum_{k=0}^{\infty} \frac{1}{a^k} \left(\frac{z_c}{w} - \frac{q_1}{w^2} - \frac{q_4}{w^5} \right)^k \right) dw \\ &= - \oint_C \left(\bar{q}_4 w^3 + \bar{q}_1 - \frac{\bar{q}_4 q_1 w}{a} + \dots \right) \left(1 + \frac{1}{a} \left(\frac{z_c}{w} - \frac{q_1}{w^2} - \frac{q_4}{w^5} \right) + \frac{1}{a^2} \left(\frac{z_c}{w} - \frac{q_1}{w^2} - \frac{q_4}{w^5} \right)^2 + \dots \right) dw \\ &= - \oint_C \left(\frac{1}{w} \left(\frac{\bar{q}_4 z_c^4}{a^4} - \frac{3\bar{q}_4 q_1 z_c^2}{a^3} + \frac{\bar{q}_4 q_1^2}{a^2} + \frac{\bar{q}_1 z_c}{a} - \frac{\bar{q}_4 q_1 z_c^2}{a^3} + \frac{\bar{q}_4 q_1^2}{a^2} \right) + \dots \right) dw \\ &= -2\pi i \left(\frac{\bar{q}_4 z_c^4}{a^4} - \frac{4\bar{q}_4 q_1 z_c^2}{a^3} + \frac{2\bar{q}_4 q_1^2}{a^2} + \frac{\bar{q}_1 z_c}{a} \right). \end{aligned} \quad (54)$$

By using $I(0) = 2\pi i (B t_c - \bar{z}_c)$ it follows that

$$a^4 B t_c = a^4 \bar{z}_c - \bar{q}_4 z_c^4 + 4a \bar{q}_4 q_1 z_c^2 - 2a^2 \bar{q}_4 q_1^2 - a^3 \bar{q}_1 z_c. \quad (55)$$

If $a = 1$ then

$$Bt_c = \bar{z}_c - \bar{q}_4 z_c^4 + 4\bar{q}_4 q_1 z_c^2 - 2\bar{q}_4 q_1^2 - \bar{q}_1 z_c, \quad (56)$$

which agrees with Eq. 34 that was found numerically.

6. Three examples of the collapse point equation

For a general case, the collapse point z_c satisfies the equation

$$0 = P(z_c) = \bar{z}_c - Bt_c + \frac{1}{2\pi i} \oint_{S(0)} \log(z - z_c) d\bar{z}, \quad (57)$$

defined at points within the object, where the integral in this equation is evaluated as a polynomial in z_c following the series expansion procedure described in the previous section. The polynomial can then be analytically extended to give an expression for $P(z_c)$ at points outside the object also. However, at points outside the object, the analytic extension will not match the value of the integral, since the enclosed residues will be different. Equation 57 is complicated: it is not analytic due to the presence of \bar{z}_c , and in general it will contain higher powers of z_c , so it is likely to have multiple solutions. To use this equation as a predictive tool, it is useful to understand the typical structure of P and know how to select the correct root. We now consider three examples that explore the structure of P in relation to the object shape.

6.1. First example: an irregular pentagonal shape

Consider an example based on Eq. 56, where the function P can be written as

$$P(z_c) = \bar{z}_c - Bt_c - \bar{q}_4 z_c^4 + 4\bar{q}_4 q_1 z_c^2 - 2\bar{q}_4 q_1^2 - \bar{q}_1 z_c, \quad (58)$$

where $t_c = 1 - |q_1|^2 - 4|q_4|^2$. Fig. 5 shows a plot of the modulus and argument of this function for the case of $a = 1$, $q_1 = \frac{1}{10} + \frac{3}{20}i$, $q_4 = \frac{1}{10} + \frac{1}{20}i$, and $B = \frac{7}{20}$. The shape of the object is also shown. There are five roots that lie outside the object. There is one root inside the object, which must be the collapse point. Furthermore, the argument in the neighborhood of the interior root rotates in the negative (anti-analytic) sense, whereas the argument near each exterior root rotates in the positive (analytic) sense. By considering the Taylor series of P at a given root, one can mathematically determine whether a root is positive-sense or negative-sense by whether $|P_z|^2 - |P_{\bar{z}}|^2$ is positive or negative, respectively. From Eq. 51, the collapse point must be given by a negative-sense root, and hence for this example there is an unambiguous choice, of the single negative-sense root within the object.

It is interesting to consider whether the other roots have physical significance. Figure 5(b) shows a zoomed-in region of the dissolution process for this example, confirming that the interior negative-sense root visible in Fig. 5(a) is indeed the collapse point. The figure also shows a nearby positive-sense root. If the system is time-integrated backward, then the boundary of the object sharpens toward the root. This leads to a cusp singularity in a finite time $t = -0.06133$, which appears similar to cusp development in related systems [17, 38]. As the cusp is approached, the matrix $M(s)$ becomes singular, and the DOP853 integrator terminates because the timestep required to keep the local error below the tolerance is smaller than what can be resolved with double precision. While the

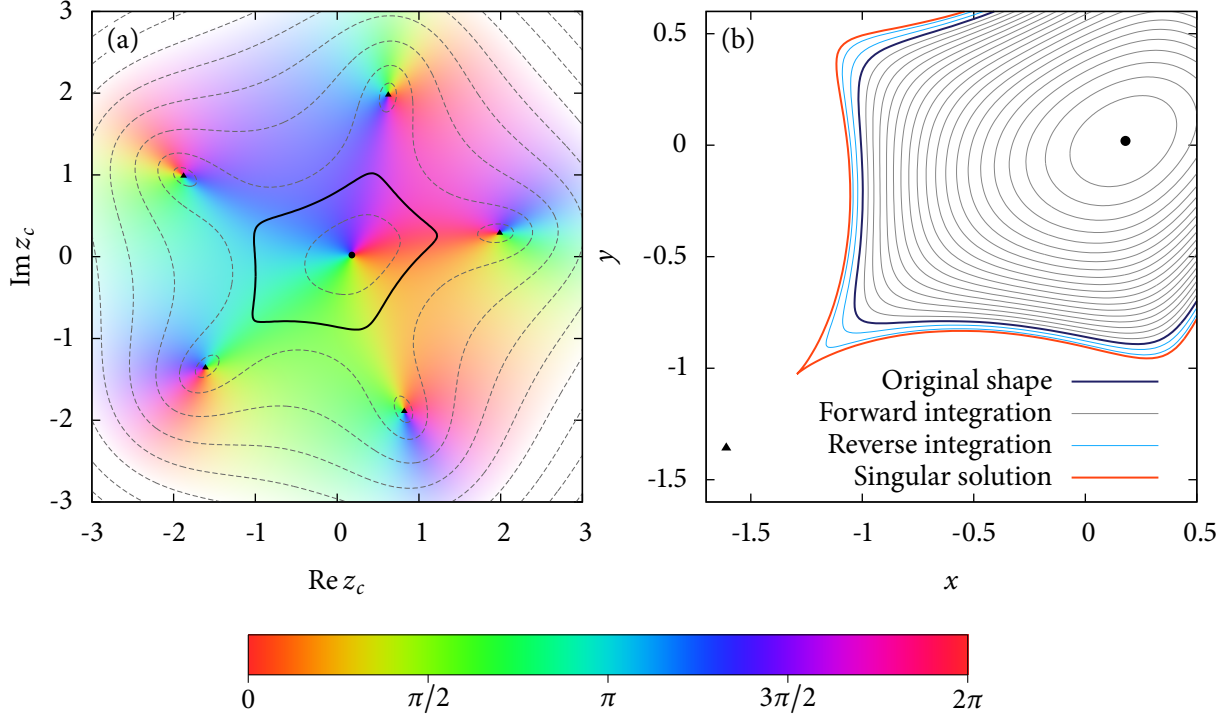


Figure 5: (a) The thick black line shows an first example object, where $a = 1$ and the only non-zero Laurent coefficients are $q_1 = \frac{1}{10} + \frac{3}{20}i$ and $q_4 = \frac{1}{10} + \frac{1}{20}i$. The colors show the argument of the function $P(z)$ for $B = \frac{7}{20}$, whose roots represent candidates for the collapse point of the object as it dissolves. The dashed lines are contours of $|P(z)|$ at values of $\frac{n^2-n+1}{2}$ for $n \in \mathbb{N}$. (b) A zoomed-in region showing forward and backward time-evolution of the object boundary at intervals of $\frac{1}{20}t_c$. The unique negative-sense root of P is shown by a circle, and one of the positive-sense roots is shown by a triangle. The four other positive-sense roots are outside the region that is plotted.

positive-sense root appears connected to the development of the cusp, it is not located exactly at the cusp, and thus it is not clear what, if any, its precise physical significance is.

A practical way to determine the root positions is to make use of a Newton–Raphson iteration, modified to take into account that P also depends on the conjugate of z_c . An appropriate Newton–Raphson iteration can be constructed by viewing P as a function of two variables z_c and \bar{z}_c , and considering the two-function system of P and \bar{P} . For a guess of the form $z_c^{(n)}$, the vector generalization of the Newton–Raphson method to give an improved guess $z_c^{(n+1)}$ is then

$$\begin{pmatrix} P_z & P_{\bar{z}} \\ \bar{P}_z & \bar{P}_{\bar{z}} \end{pmatrix} \begin{pmatrix} z_c^{(n+1)} - z_c^{(n)} \\ \bar{z}_c^{(n+1)} - \bar{z}_c^{(n)} \end{pmatrix} = - \begin{pmatrix} P \\ \bar{P} \end{pmatrix}, \quad (59)$$

which leads to the two equations

$$P_z(z_c^{(n+1)} - z_c^{(n)}) + P_{\bar{z}}(\bar{z}_c^{(n+1)} - \bar{z}_c^{(n)}) = -P, \quad (60)$$

$$\bar{P}_z(z_c^{(n+1)} - z_c^{(n)}) + \bar{P}_{\bar{z}}(\bar{z}_c^{(n+1)} - \bar{z}_c^{(n)}) = -\bar{P}. \quad (61)$$

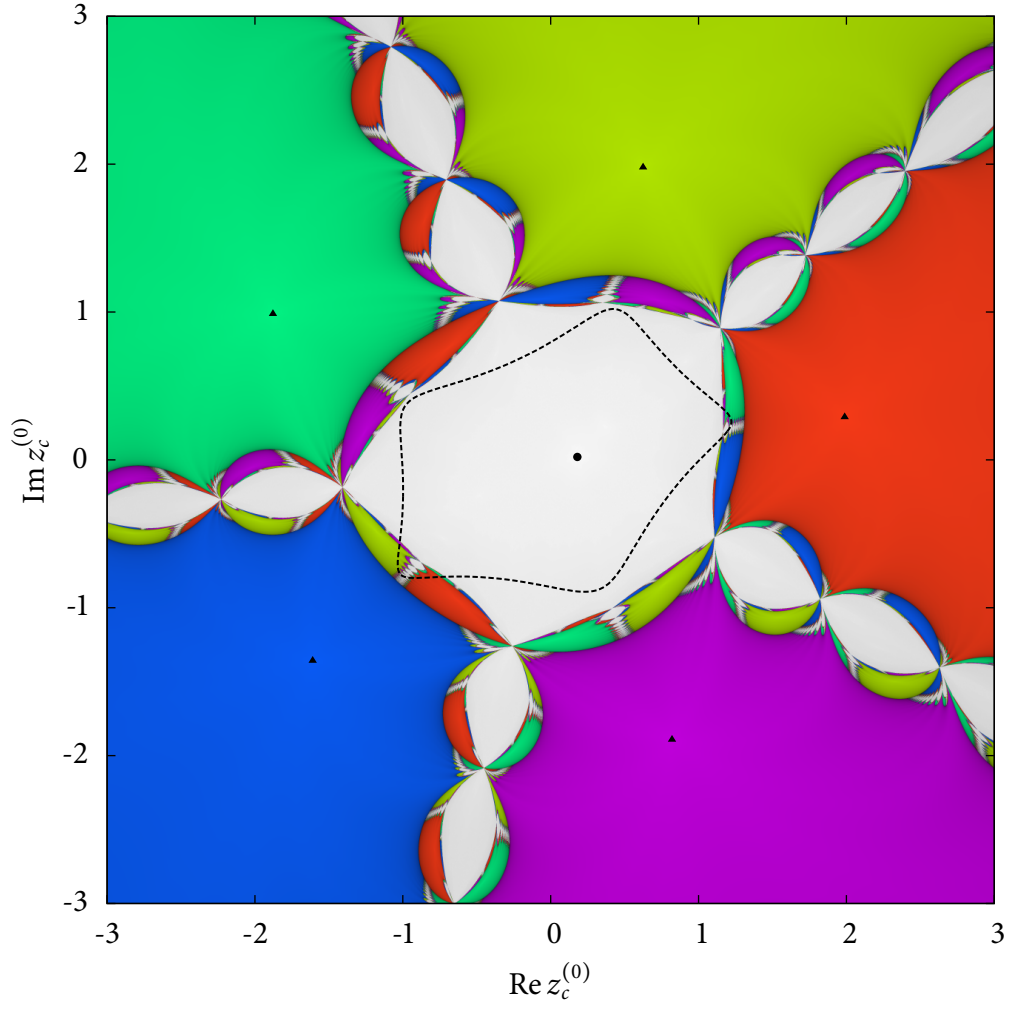


Figure 6: Plot showing which root of P a Newton–Raphson iteration will converge to when starting at $z_c^{(0)}$, for the example configuration given in Fig. 5. The five positive-sense roots of P are shown by small black triangles, and the unique negative-sense root is shown by a small black circle. Each point is colored according to the argument of the root that it converges to, with the central root being shown in white. Darker shades show regions that require more iterations to converge.

Substituting Eq. 61 into Eq. 60 to eliminate $(\bar{z}_c^{(n+1)} - \bar{z}_c^{(n)})$ gives the iterative equation

$$z_c^{(n+1)} = z_c^{(n)} + \frac{\bar{P}P_z - P\bar{P}_z}{|P_z|^2 - |\bar{P}_z|^2}. \quad (62)$$

As expected, if $P_z = 0$, then this equation reduces to the standard complex Newton–Raphson iteration.

Figure 6 shows a plot of which root the Newton–Raphson iteration will converge to as a function of the starting guess $z_c^{(0)}$. As is typical for Newton–Raphson iterations of complex functions, the plot has a fractal structure, with large basins of attraction surrounding each root. However, the plot has some distinctly different features to usual Newton fractals [39, 40] arising from the vector generalization of the iteration to non-analytic functions. In particular, the denominator $|P_z|^2 - |\bar{P}_z|^2$ featuring in Eq. 62 is zero on a one-dimensional loop of points surrounding the central root. Any starting guess that approaches this loop will therefore undergo a very large initial step. In Fig. 6, this loop forms the dividing line between the five outer colored basins and the central region. Due to the self-similarity of the fractal, the structure surrounding this loop is replicated in other parts of the plot. This is in noticeable contrast to the regular Newton fractal for an analytic function $f(z)$, where the iteration becomes singular only at a zero-dimensional set of points where $f'(z) = 0$.

On Figure 6, the object boundary is shown by the dashed black line, and it is almost entirely contained within the central white region, meaning that a starting guess within the object is likely to converge to the collapse point; if the guess is chosen near the center of the object, such as at q_0 , the iteration converges very rapidly and reliably. However the plot also indicates that for several small regions inside the object (e.g. near the bottom left corner) the Newton–Raphson method may converge to one of the exterior roots.

6.2. Second example: a dumbbell-shaped object dividing in two

Figure 7(a) shows the dissolution process for the case of a long dumbbell-shaped object, where $a = 1$, $q_1 = -\frac{7}{10}$, $q_3 = -\frac{1}{4}$, $B = \frac{3}{5}$, and all other Laurent series coefficients are zero. In this case, the thin vertical sliver dissolves away leaving two separated fragments. While the system can be time-integrated past this point with $M(s)$ remaining non-singular, the contour begins to overlap with itself, thus losing physical validity. The function P for this example is

$$P(z_c) = \bar{z}_c - Bt_c - \bar{q}_3z_c^3 + 3\bar{q}_3q_1z_c - \bar{q}_1z_c,$$

where $t_c = 1 - |q_1|^2 - 3|q_3|$. The structure of $P(z_c)$ and its roots are plotted in Fig. 7(b). The function P has two negative-sense roots in either end of the dumbbell, four exterior positive-sense roots, and one positive-sense root on the vertical sliver. This example also highlights that the non-analyticity of P significantly increases its complexity. The last four terms of P form an analytic cubic function in z_c , which could have at most three distinct roots, but adding the anti-analytic \bar{z}_c increases the number of roots to seven.

While more complicated than the previous example, the positions of the roots appear to be physically reasonable, with one negative-sense root appearing in each end of the dumbbell. The central positive-sense root appears to be associated with the position where the vertical sliver dissolves. However, close inspection reveals that its position is not perfectly aligned with the point where the two sides of the object first come into contact. Instead, it appears to mark the center of the inverted

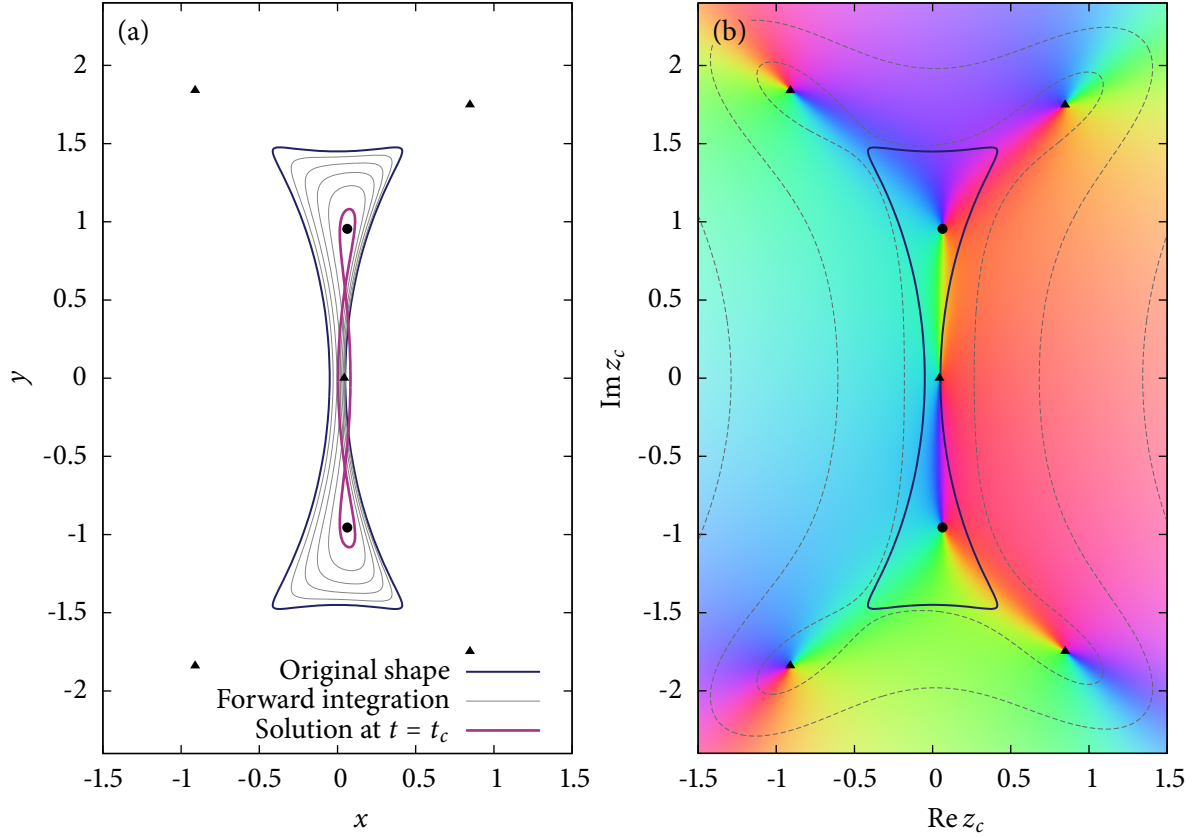


Figure 7: (a) Time-evolution of a dumbbell-shaped object described by $a = 1$, $q_1 = -\frac{7}{10}$, $q_3 = -\frac{1}{4}$, $B = \frac{3}{5}$, and all other Laurent series coefficients are zero. The gray curves are plotted at intervals of $\frac{1}{5}t_c$. Positive-sense roots of the function P are shown by triangles, and negative-sense roots are shown by circles. (b) The structure of the corresponding function P , with the dashed lines corresponding to contours of $|P(z)|$ at $\frac{n^2-n+1}{4}$ for $n \in \mathbb{N}$, and the colors corresponding to the argument using the key given in Fig. 5.

section of the contour at $t = t_c$. Figure 8 shows a plot of which root the Newton–Raphson iteration converges to, depending on the starting guess. For starting points $z_c^{(0)}$ within the object, most will converge to the two negative-sense roots or the central positive-sense root. The denominator $|P_z|^2 - |P_{\bar{z}}|^2$ in Eq. 62 vanishes on two approximate ellipses surrounding each negative-sense root.

While it is not physically valid to simulate the dissolution of the object to collapse, this example highlights that the structure of P and the position of its roots may be more complicated than in the previous example considered, and thus any further mathematical analyses would have to take into account this possibility.

6.3. Third example: transitions in behavior as flow strength is altered

The final example is a three-pronged object given by the initial non-zero Laurent coefficients $a = 1$, $q_2 = -\frac{49}{100}$, $q_5 = -\frac{17}{100}$, $q_8 = -\frac{3}{40}$, $q_{11} = -\frac{27}{1000}$, and $q_{14} = -\frac{3}{500}$. Unlike the previous two examples, the collapse point equation is difficult to determine manually due to the large number of Laurent

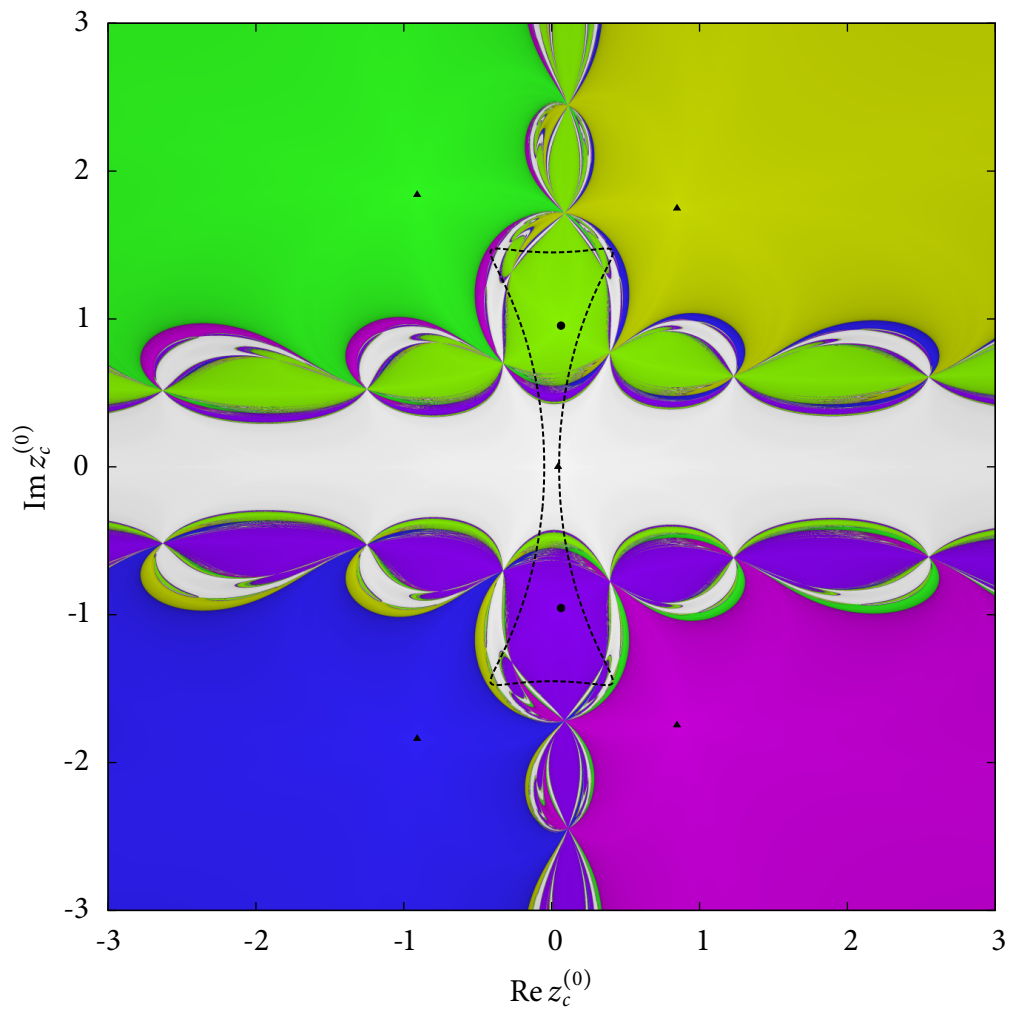


Figure 8: Plot showing which root of P a Newton–Raphson iteration will converge to when starting at $z_c^{(0)}$, for the dumbbell-shaped example. The five positive-sense roots of P are shown by black triangles, and the two negative-sense roots are shown by black circles. Each point is colored according to the argument of the root that it converges to, with the central root being shown in white. Darker shades show regions that require more iterations to converge.

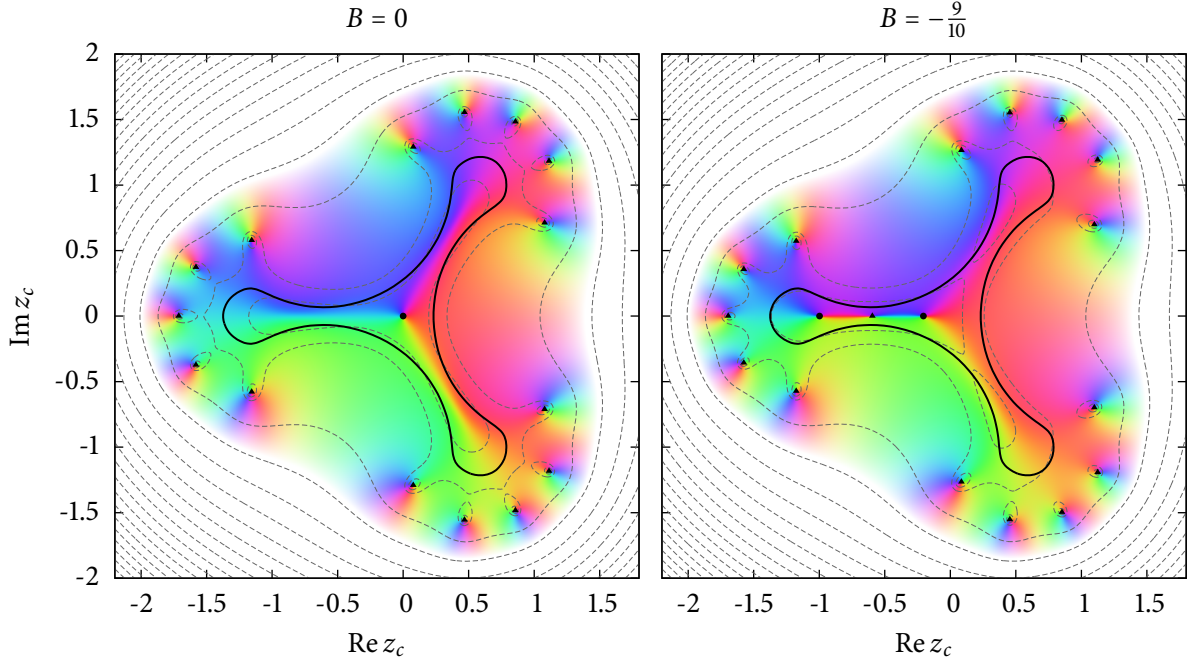


Figure 9: Plot of the collapse point equation $P(z_c)$ for the three-pronged object for (a) $B = 0$, and (b) $B = -\frac{9}{10}$. The colors correspond to the argument of $P(z)$ using the same scale as Fig. 5. The positive-sense roots are shown with black triangles and the negative-sense roots are shown with black circles. The thick black line shows the boundary of the object. The thin dashed grey lines are contours of $|P(z)|$ at $\frac{1}{4}(n^4 + 1)$ for $n \in \mathbb{N}_0$.

series terms that must be considered. However, a computer code was written that found it to be

$$\begin{aligned}
 P(z_c) = & \bar{z}_c - Bt_c - \bar{q}_{14}z_c^{14} + z_c^{11}(-\bar{q}_{11} + 14\bar{q}_{14}q_2) + z_c^8(-\bar{q}_8 + 11\bar{q}_{11}q_2 + 14\bar{q}_{14}q_5 - 63\bar{q}_{14}q_2^2) \\
 & + z_c^5(-\bar{q}_5 + 8\bar{q}_8q_2 + 11\bar{q}_{11}q_5 + 14\bar{q}_{14}q_8 - 33\bar{q}_{11}q_2^2 - 84\bar{q}_{14}q_2q_5 + 98\bar{q}_{14}q_2^3) \\
 & + z_c^2(-\bar{q}_2 + 5\bar{q}_5q_2 + 8\bar{q}_8q_5 + 11\bar{q}_{11}q_8 + 14\bar{q}_{14}q_{11} - 12\bar{q}_8q_2^2 - 32\bar{q}_{11}q_2q_5 \\
 & - 42\bar{q}_{14}q_2q_8 - 21\bar{q}_{14}q_5^2 + 22\bar{q}_{11}q_2^3 + 84\bar{q}_{14}q_2^2q_5 - 35\bar{q}_{14}q_2^4). \tag{63}
 \end{aligned}$$

The left panel of Fig. 9 shows the structure of the solution polynomial when $B = 0$. Each of the three prongs is surrounded by five positive-sense roots, and there is a single negative-sense root at the origin. The magnitude of P within the object is small, so that most of the object lies within the region $|P(z_c)| < \frac{1}{4}$, meaning that an alteration of the flow strength could alter the function's roots. The right panel shows the function P when $B = -\frac{9}{10}$, corresponding to a strong flow from the right. In this case a new pair of positive-sense and negative-sense roots appear on the real axis, resulting in a similar root arrangement to Fig. 7(b).

Figure 10 shows the dissolution process for three different cases of B , for a zoomed-in region centered on one of the prongs. The top panel shows the case when $B = 0$, where the dissolution process proceeds normally and the object collapses at the single negative-sense root at the origin.

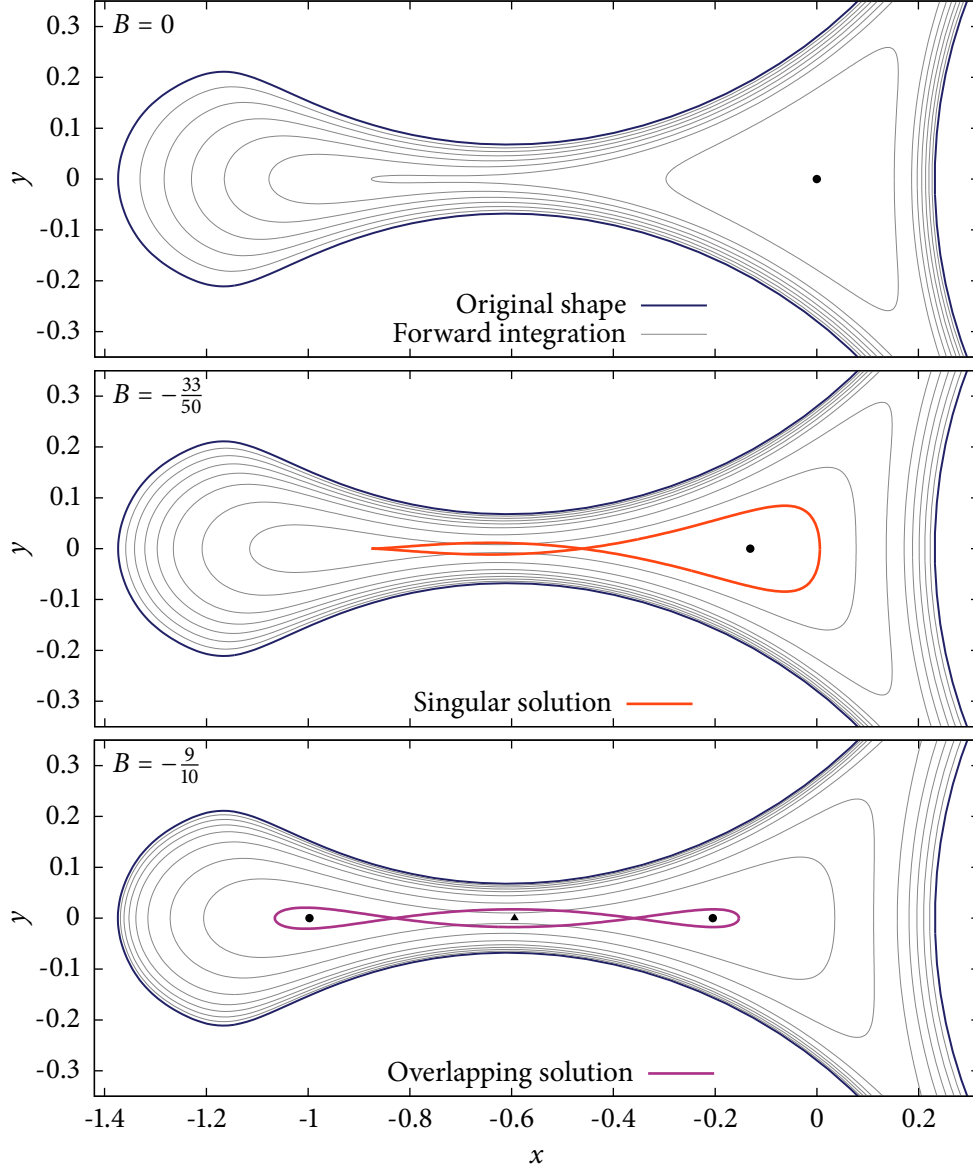


Figure 10: Zoomed-in plot of the dissolution process for the three-pronged object, for three different values of the flow strength B , showing snapshots of the object boundary at intervals of $\frac{t_c}{8}$ where $t_c = 0.1608885$. The positive-sense roots are shown with black triangles and the negative-sense roots are shown with black circles. For $B = 0$, the object collapses to the origin at $t = t_c$. For $B = -\frac{33}{50}$, the object boundary overlaps and then a singular solution with a cusp forms at $t = 0.1550602$. For $B = -\frac{9}{10}$ the boundary forms an overlapping curve at $t = t_c$.

Since the physical model given in Eqs. 1, 2, & 3 tends to rapidly dissolve sharply curved boundaries, the three prongs of the object dissolve rapidly enough that they remain connected to each other.

For the case of $B = \frac{9}{10}$ shown in the bottom panel of Fig. 10 the situation is different. The incorporation of flow into the evolution equation of Eq. 11 causes the thin part of the prong to dissolve more rapidly than its end, meaning that in this case, the object becomes disconnected into two regions. The behavior is similar to the previous example, where the object boundary overlaps with itself. At $t = t_c$, the object boundary loops around the two negative-sense roots and the positive-sense root in the same manner as Fig. 7(a). This example highlights that only altering flow strength is sufficient to cause a transition in the behavior of the dissolution process.

The transition in behavior is linked with the formation of the new roots in Fig. 9 as B is changed from 0 to $-\frac{9}{10}$. However, the middle panel of Fig. 10 for an intermediate flow strength of $B = -\frac{33}{50}$ shows that this transition is more complicated. In this case, there is only a single negative-sense root in P . However, during time-evolution, the object boundary first overlaps with itself, and then the left loop shrinks to zero size, leading to a singular solution with an inverted cusp at time $t = 0.1550602 < t_c$.

We carried out a systematic sweep over the flow strengths over the range from $B = 0$ to $B = -1$: initially the object collapses to a single point, at $B \approx -0.233$ an inverted cusp forms, and at $B \approx -0.794$ a second negative-sense root forms, when the left loop is large enough to persist until t_c . This result highlights that dissolution process can transition between at least three distinct behaviors. Furthermore, the result for $B = -\frac{33}{50}$ shows that even if P only has a single negative-sense root, the dissolution process may not be straightforward, and may lead to an overlapping boundary or a singular solution.

Figure 11 shows which roots the modified Newton–Raphson iteration will converge to, for the case of $B = 0$. The plot has an intricate structure and there are many small, distinct regions that converge to the central root. The denominator $|P_z|^2 - |P_{\bar{z}}|^2$ in Eq. 62 vanishes on a small loop surrounding the central root, and starting guesses near this loop are colored in darker shades, indicating that the root-finding algorithm takes many iterations to converge. The plot highlights the difficulty of finding the particular roots of interest in a general case.

7. Conclusion

In this paper, we studied a model of object dissolution within a two-dimensional potential flow, and we created a numerical implementation of it that allowed us to simulate the dissolution process for arbitrary objects described in terms of a Laurent series. The simulations revealed an exact relationship where the collapse point z_c is the root of a non-analytic function given in the terms of the Laurent coefficients and the flow strength. This relationship was subsequently derived analytically, but it is unlikely that it would have been discovered without the numerical results as a guide. These simulations made use of a high-order numerical method, and while these methods are often difficult or too computationally expensive to apply to real engineering problems, this work demonstrates their power in mathematical analysis: the numerical results for the collapse point are accurate enough to infer the underlying exact relationship with reasonable confidence. There are other examples where high-accuracy numerical methods have been used for similar purposes, such as demonstrating the existence of special solutions to equations [41, 42] or to discovering universal behavior [43].

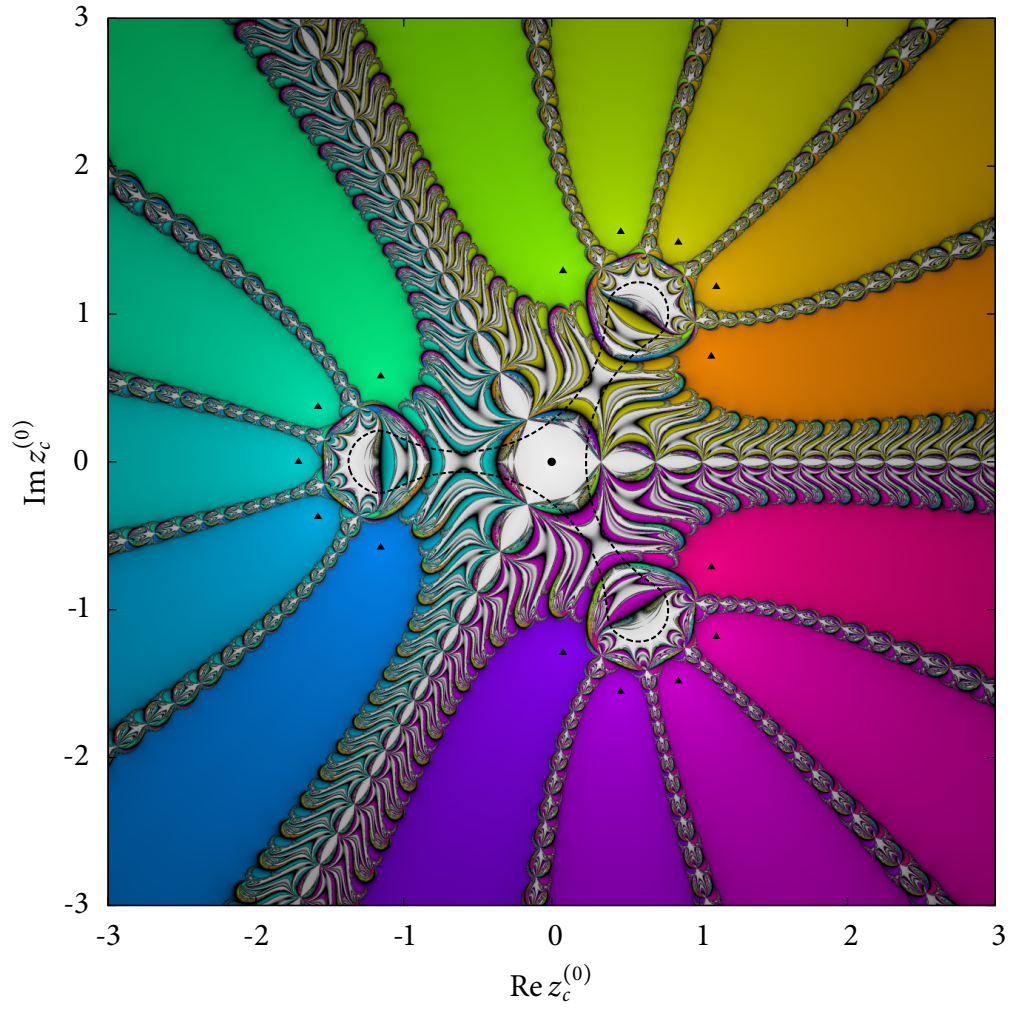


Figure 11: Plot showing which root of the solution polynomial P a Newton–Raphson iteration will converge to when starting at $z_c^{(0)}$, for the three-pronged object when $B = 0$. The fifteen positive-sense roots of P are shown by black triangles, and the single negative-sense root at the origin is shown by a black circle. Each point is colored according to the argument of the root that it converges to, with the central root being shown in white. Darker shades show regions that require more iterations to converge.

The examples of Section 6 create some interesting theoretical questions for future investigation. We expect that the first example of the pentagonal shape (Subsec. 6.1) represents typical behavior for most objects, where the dissolution process is well-defined, the object collapses to a single point, and the collapse point function $P(z_c)$ has a single negative-sense root. More specifically, we expect this to be true for a large class of cases where the q_j are small in comparison to a , and hence the collapse point function in Eq. 57 will be dominated by the \bar{z}_c term and thus likely to have a single anti-analytic root close to the origin. However, the second example shows that not all cases may lead to this typical behavior, and object may dissolve into multiple fragments, with $P(z_c)$ gaining additional negative-sense roots. The third example adds a further complication, showing that only a minor alteration of the flow strength B can lead to cases where dissolution is not well-defined, even though $P(z_c)$ still has a single negative-sense root. Taken together, these results motivate two further questions: (A) what the conditions on the initial modes for P to have a single anti-analytic root, and (B) what are the conditions on the initial modes for the dissolution process to be well-defined and for the object to collapse to a single point?

If questions A and B can be answered, then a further direction would be to identify a procedure capable of determining the collapse point with absolute certainty. The modified Newton–Raphson that was introduced in Subsec. 6.1 is very efficient at identifying roots, but it is difficult to determine *a priori* which root it will converge to, and plots of the convergence as a function of the starting guess exhibit a fractal structure as is typical for complex Newton–Raphson iterations. Furthermore, the non-analyticity of $P(z_c)$ creates some difficulties whereby the total number of roots exhibits fundamentally different behavior than for analytic functions. An analytic cubic polynomial in z_c has exactly three roots (when counted with multiplicity) but the addition of a non-analytic \bar{z}_c as in the second example (Subsec. 6.2) leads to seven roots, five of which are positive-sense and two of which are negative-sense. By using a winding argument, considering the curve $P(Re^{i\theta})$ as $R \rightarrow \infty$, we expect that $n_+ - n_- = N$ where N is the maximum non-zero mode, and n_{\pm} are the number of positive-sense and negative-sense roots. We also consider the Newton–Raphson fractals to be interesting in their own right, since they have a fundamentally different structure than typical Newton–Raphson fractals due to the one-dimensional set of points where the denominator in Eq. 62 vanishes. There is an interesting correspondence whereby each object has an associated fractal.

A variety of generalizations to the dissolution model could also be explored. The simple form of the right hand side of Eq. 11 was based on asymptotic considerations of the concentration profile in the low Péclet number limit, but the numerical method could be extended to more complex growth laws where higher powers of $\cos \theta$ and $\sin \theta$ are present. Since the derivation of the collapse point function is not highly dependent on the simple form of Eq. 11, it may be possible to generalize this to more complex growth laws as well. Another extension would be to the case of regular polyhedral objects, which could be approximated using a large number of terms in a Laurent series.

The second and third examples of Subsecs. 6.2 and 6.3 show that in some cases an object may dissolve into several components. In the current numerical method the dissolution process cannot be accurately simulated beyond the point where multiple fragments form, but it may be possible to extend the simulation to this case by using recent advances in conformal mapping for multiply connected domains [44, 45, 46, 47]. The dissolution model is a particularly interesting example, since the physical process involves a single domain smoothly transitioning into two. We aim to investigate

all of these interesting directions in future work.

Appendix A. Component form of the time-evolution equation

The numerical method introduced in Section 3 is based upon equating the different sine and cosine components of Eq. 13, which is

$$-1 + Ba \cos \theta = \text{Re} \left(\left[a e^{-i\theta} - \sum_{n=0}^N n(b_n - i c_n) e^{in\theta} \right] \left[\dot{a} e^{i\theta} + \sum_{n=0}^N (\dot{b}_n + i \dot{c}_n) e^{-in\theta} \right] \right).$$

Multiplying out these power series yields

$$\begin{aligned} -1 + Ba \cos \theta = & \text{Re} \left(a \dot{a} - \dot{a} \sum_{n=0}^N n(b_n - i c_n) e^{i(n+1)\theta} + a \sum_{m=0}^N (\dot{b}_m + i \dot{c}_m) e^{i(m+1)\theta} \right. \\ & \left. - \sum_{n=0}^N \sum_{m=0}^N n(b_n - i c_n)(\dot{b}_m + i \dot{c}_m) e^{i(n-m)\theta} \right). \end{aligned} \quad (\text{A.1})$$

Taking the real component of the bracketed term yields

$$\begin{aligned} -1 + Ba \cos \theta = & a \dot{a} - \sum_{n=0}^N \sum_{m=0}^N n \left[(b_n \dot{b}_m + c_n \dot{c}_m) \cos(n-m)\theta + (c_n \dot{b}_m - b_n \dot{c}_m) \sin(n-m)\theta \right] \\ & + a \sum_{m=0}^N (\dot{b}_m \cos(m+1)\theta + \dot{c}_m \sin(m+1)\theta) \\ & - \dot{a} \sum_{n=0}^N (b_n \cos(n+1)\theta + c_n \sin(n+1)\theta). \end{aligned} \quad (\text{A.2})$$

Collecting terms with factors of sine and cosine yields

$$\begin{aligned} -1 + Ba \cos \theta = & a \dot{a} - \sum_{n=0}^N n(b_n \dot{b}_n + c_n \dot{c}_n) \\ & - \dot{a} \sum_{n=1}^{N+1} (n-1)(b_{n-1} \cos n\theta + c_{n-1} \sin n\theta) + a \sum_{m=1}^{N+1} (\dot{b}_{m-1} \cos m\theta + \dot{c}_{m-1} \sin m\theta) \\ & - \sum_{k=1}^N \sum_{m=0}^{N-k} \left[(m+k)(b_{m+k} \dot{b}_m + c_{m+k} \dot{c}_m) \cos k\theta \right. \\ & + (m+k)(c_{m+k} \dot{b}_m - b_{m+k} \dot{c}_m) \sin k\theta + m(b_m \dot{b}_{m+k} + c_m \dot{c}_{m+k}) \cos k\theta \\ & \left. - m(c_m \dot{b}_{m+k} - b_m \dot{c}_{m+k}) \sin k\theta \right]. \end{aligned} \quad (\text{A.3})$$

Equating the terms with different factors of sine and cosine yields Eqs. 14, 15, 16, and 17, which together form the linear system that is used in the numerical integration method.

Bibliography

- [1] M. Burden, J. Hunt, Cellular and dendritic growth. I, *Journal of Crystal Growth* 22 (2) (1974) 99–108. [doi:10.1016/0022-0248\(74\)90126-2](https://doi.org/10.1016/0022-0248(74)90126-2).
- [2] D. J. Wollkind, R. Sriranganathan, D. B. Oulton, Interfacial patterns during plane front alloy solidification, *Physica D: Nonlinear Phenomena* 12 (1–3) (1984) 215–240. [doi:10.1016/0167-2789\(84\)90526-8](https://doi.org/10.1016/0167-2789(84)90526-8).
- [3] J. A. Sethian, J. Strain, Crystal growth and dendritic solidification, *Journal of Computational Physics* 98 (2) (1992) 231–253. [doi:10.1016/0021-9991\(92\)90140-T](https://doi.org/10.1016/0021-9991(92)90140-T).
- [4] M. Theillard, F. Gibou, T. Pollock, A sharp computational method for the simulation of the solidification of binary alloys (2014). [doi:10.1007/s10915-014-9895-0](https://doi.org/10.1007/s10915-014-9895-0).
- [5] G. Wranglén, Dendrites and growth layers in the electrocrystallization of metals, *Electrochimica Acta* 2 (1–3) (1960) 130–143. [doi:10.1016/0013-4686\(60\)87010-7](https://doi.org/10.1016/0013-4686(60)87010-7).
- [6] R. M. Brady, R. C. Ball, Fractal growth of copper electrodeposits, *Nature* 309 (5965) (1984) 225–229. [doi:10.1038/309225a0](https://doi.org/10.1038/309225a0).
- [7] D. A. Kessler, J. Koplik, H. Levine, Numerical simulation of two-dimensional snowflake growth, *Phys. Rev. A* 30 (1984) 2820–2823. [doi:10.1103/PhysRevA.30.2820](https://doi.org/10.1103/PhysRevA.30.2820).
- [8] L. Gránásy, T. Pusztai, T. Börzsönyi, J. A. Warren, J. F. Douglas, A general mechanism of polycrystalline growth, *Nature Materials* 3 (9) (2004) 645–650. [doi:10.1038/nmat1190](https://doi.org/10.1038/nmat1190).
- [9] J. S. Langer, Instabilities and pattern formation in crystal growth, *Rev. Mod. Phys.* 52 (1980) 1–28. [doi:10.1103/RevModPhys.52.1](https://doi.org/10.1103/RevModPhys.52.1).
- [10] E. Ben-Jacob, P. Garik, The formation of patterns in non-equilibrium growth, *Nature* 343 (6258) (1990) 523–530. [doi:10.1038/343523a0](https://doi.org/10.1038/343523a0).
- [11] W. W. Mullins, R. F. Sekerka, Morphological stability of a particle growing by diffusion or heat flow, *Journal of Applied Physics* 34 (2) (1963) 323–329. [doi:10.1063/1.1702607](https://doi.org/10.1063/1.1702607).
- [12] E. Ben-Jacob, N. Goldenfeld, J. S. Langer, G. Schön, Dynamics of interfacial pattern formation, *Phys. Rev. Lett.* 51 (1983) 1930–1932. [doi:10.1103/PhysRevLett.51.1930](https://doi.org/10.1103/PhysRevLett.51.1930).
- [13] T. A. Witten, L. M. Sander, Diffusion-limited aggregation, a kinetic critical phenomenon, *Phys. Rev. Lett.* 47 (1981) 1400–1403. [doi:10.1103/PhysRevLett.47.1400](https://doi.org/10.1103/PhysRevLett.47.1400).
- [14] P. Meakin, Effects of particle drift on diffusion-limited aggregation, *Phys. Rev. B* 28 (1983) 5221–5224. [doi:10.1103/PhysRevB.28.5221](https://doi.org/10.1103/PhysRevB.28.5221).
- [15] P. Meakin, Cluster-particle aggregation with fractal (levy flight) particle trajectories, *Phys. Rev. B* 29 (1984) 3722–3725. [doi:10.1103/PhysRevB.29.3722](https://doi.org/10.1103/PhysRevB.29.3722).

- [16] L. Paterson, Diffusion-limited aggregation and two-fluid displacements in porous media, *Phys. Rev. Lett.* 52 (1984) 1621–1624. [doi:10.1103/PhysRevLett.52.1621](https://doi.org/10.1103/PhysRevLett.52.1621).
- [17] B. Shraiman, D. Bensimon, Singularities in nonlocal interface dynamics, *Phys. Rev. A* 30 (1984) 2840–2842. [doi:10.1103/PhysRevA.30.2840](https://doi.org/10.1103/PhysRevA.30.2840).
- [18] P. G. Saffman, G. Taylor, The penetration of a fluid into a porous medium or hele-shaw cell containing a more viscous liquid, *Proceedings of the Royal Society of London. Series A. Mathematical and Physical Sciences* 245 (1242) (1958) 312–329. [doi:10.1098/rspa.1958.0085](https://doi.org/10.1098/rspa.1958.0085).
- [19] D. Bensimon, L. P. Kadanoff, S. Liang, B. I. Shraiman, C. Tang, Viscous flows in two dimensions, *Rev. Mod. Phys.* 58 (1986) 977–999. [doi:10.1103/RevModPhys.58.977](https://doi.org/10.1103/RevModPhys.58.977).
- [20] M. J. Feigenbaum, I. Procaccia, B. Davidovich, Dynamics of finger formation in Laplacian growth without surface tension, *Journal of Statistical Physics* 103 (5–6) (2001) 973–1007. [doi:10.1023/A:1010313106449](https://doi.org/10.1023/A:1010313106449).
- [21] F. Barra, B. Davidovitch, I. Procaccia, Iterated conformal dynamics and Laplacian growth, *Phys. Rev. E* 65 (2002) 046144. [doi:10.1103/PhysRevE.65.046144](https://doi.org/10.1103/PhysRevE.65.046144).
- [22] T. C. Halsey, Diffusion-limited aggregation: A model for pattern formation, *Physics Today* 53 (11) (2000) 36. [doi:10.1063/1.1333284](https://doi.org/10.1063/1.1333284).
- [23] M. Hastings, L. Levitov, Laplacian growth as one-dimensional turbulence, *Physica D: Nonlinear Phenomena* 116 (1–2) (1998) 244–252. [doi:10.1016/S0167-2789\(97\)00244-3](https://doi.org/10.1016/S0167-2789(97)00244-3).
- [24] B. Davidovitch, M. J. Feigenbaum, H. G. E. Hentschel, I. Procaccia, Conformal dynamics of fractal growth patterns without randomness, *Phys. Rev. E* 62 (2000) 1706–1715. [doi:10.1103/PhysRevE.62.1706](https://doi.org/10.1103/PhysRevE.62.1706).
- [25] M. Z. Bazant, J. Choi, B. Davidovitch, Dynamics of conformal maps for a class of non-Laplacian growth phenomena, *Phys. Rev. Lett.* 91 (2003) 045503. [doi:10.1103/PhysRevLett.91.045503](https://doi.org/10.1103/PhysRevLett.91.045503).
- [26] M. Z. Bazant, Conformal mapping of some non-harmonic functions in transport theory, *Proceedings of the Royal Society of London. Series A: Mathematical, Physical and Engineering Sciences* 460 (2045) (2004) 1433–1452. [doi:10.1098/rspa.2003.1218](https://doi.org/10.1098/rspa.2003.1218).
- [27] J. Choi, D. Margetis, T. M. Squires, M. Z. Bazant, Steady advection–diffusion around finite absorbers in two-dimensional potential flows, *Journal of Fluid Mechanics* 536 (2005) 155–184. [doi:10.1017/S0022112005005008](https://doi.org/10.1017/S0022112005005008).
- [28] B. Davidovitch, J. Choi, M. Z. Bazant, Average shape of transport-limited aggregates, *Phys. Rev. Lett.* 95 (2005) 075504. [doi:10.1103/PhysRevLett.95.075504](https://doi.org/10.1103/PhysRevLett.95.075504).
- [29] J. Choi, D. Crowdy, M. Z. Bazant, Diffusion-limited aggregation on curved surfaces, *EPL (Europhysics Letters)* 91 (4) (2010) 46005. [doi:10.1209/0295-5075/91/46005](https://doi.org/10.1209/0295-5075/91/46005).

- [30] P. Meakin, J. M. Deutch, The formation of surfaces by diffusion limited annihilation, *The Journal of Chemical Physics* 85 (4) (1986) 2320–2325. doi:10.1063/1.451129.
- [31] J. Krug, P. Meakin, Kinetic roughening of Laplacian fronts, *Phys. Rev. Lett.* 66 (1991) 703–706. doi:10.1103/PhysRevLett.66.703.
- [32] G. F. Lawler, M. Bramson, D. Griffeath, Internal diffusion limited aggregation, *The Annals of Probability* 20 (4) (1992) 2117–2140. doi:10.2307/2244742.
- [33] M. Z. Bazant, Interfacial dynamics in transport-limited dissolution, *Phys. Rev. E* 73 (2006) 060601. doi:10.1103/PhysRevE.73.060601.
- [34] E. Hairer, S. P. Nørsett, G. Wanner, *Solving Ordinary Differential Equations I: Nonstiff Problems*, Springer, Berlin, 1993.
- [35] E. Hairer, S. P. Nørsett, G. Wanner, *Solving Ordinary Differential Equations II: Stiff and Differential-Algebraic Problems*, Springer, Berlin, 1996.
- [36] E. Anderson, Z. Bai, C. Bischof, S. Blackford, J. Demmel, J. Dongarra, J. Du Croz, A. Greenbaum, S. Hammarling, A. McKenney, D. Sorensen, *LAPACK Users' Guide*, 3rd Edition, Society for Industrial and Applied Mathematics, Philadelphia, PA, 1999.
- [37] J. Dormand, P. Prince, [Practical runge–kutta processes](#), *SIAM Journal on Scientific and Statistical Computing* 10 (5) (1989) 977–989. doi:10.1137/0910057. URL [10.1137/0910057](#)
- [38] S. Howison, Cusp development in Hele–Shaw flow with a free surface, *SIAM Journal on Applied Mathematics* 46 (1) (1986) 20–26. doi:10.1137/0146003.
- [39] B. B. Mandelbrot, *The Fractal Geometry of Nature*, W. H. Freeman and Company, 1982.
- [40] H.-O. Peitgen, D. Saupe, *The Science of Fractal Images*, Springer, 1988.
- [41] J. Wilkening, Breakdown of self-similarity at the crests of large-amplitude standing water waves, *Phys. Rev. Lett.* 107 (2011) 184501. doi:10.1103/PhysRevLett.107.184501.
- [42] C. H. Rycroft, J. Wilkening, Computation of three-dimensional standing water waves, *Journal of Computational Physics* 255 (2013) 612–638. doi:10.1016/j.jcp.2013.08.026.
- [43] G. I. Barenblatt, P. J. M. Monteiro, C. H. Rycroft, On a boundary layer problem related to the gas flow in shales, *Journal of Engineering Mathematics* 84 (1) (2014) 11–18. doi:10.1007/s10665-012-9612-7.
- [44] T. Delillo, A. Elcrat, J. Pfaltzgraff, Schwarz–Christoffel mapping of multiply connected domains, *Journal d'Analyse Mathématique* 94 (1) (2004) 17–47. doi:10.1007/BF02789040.

- [45] D. Crowdy, The Schwarz–Christoffel mapping to bounded multiply connected polygonal domains, *Proceedings of the Royal Society A: Mathematical, Physical and Engineering Science* 461 (2061) (2005) 2653–2678. [doi:10.1098/rspa.2005.1480](https://doi.org/10.1098/rspa.2005.1480).
- [46] T. K. DeLillo, Schwarz–Christoffel mapping of bounded, multiply connected domains, *Computational Methods and Function Theory* 6 (2) (2006) 275–300. [doi:10.1007/BF03321615](https://doi.org/10.1007/BF03321615).
- [47] D. Crowdy, Schwarz–Christoffel mappings to unbounded multiply connected polygonal regions, *Mathematical Proceedings of the Cambridge Philosophical Society* 142 (2007) 319–339. [doi:10.1017/S0305004106009832](https://doi.org/10.1017/S0305004106009832).